Ph.D. Dissertation

Experimental investigation of oncological biomarker detection by nanoelectrokinetic selective preconcentration

이온 농도 분극 현상을 이용한 나노전기동역학적 유전자 검출

August 2021

Department of Electrical and Computer Engineering
College of Engineering
Seoul National University

Sangjun Lee

Experimental Investigation of Oncological Biomarker Detection by Nanoelectrokinetic Selective Preconcentration

지도교수 김 성 재

이 논문을 공학박사 학위논문으로 제출함

2021 년   8 월

서울대학교 대학원
전기 · 정보 공학부
이 상 준

이상준의 공학박사 학위논문을 인준함
2021 년   8 월

위 원 장	홍 용 택
부위원장	김 성 재
위 원	김 호 영
위 원	전 누 리
위 원	성 건 용

1

Abstract

Microfluidic systems have been in the spotlight since the 1990s due to various advantages from miniaturization such as highly efficient sample analysis and ease of system control, *etc*. Meanwhile, the advance of nanotechnology (especially for nano structure fabrication) has accelerated the research on micro/nanofluidic platform and its applications. In the sub- mm region, new physico-chemical phenomena that were not observed in other regions were discovered. Among them, selective permeability by electrical double layer overlap is considered as a most important feature. Using this selective permeability, researches on various application fields are being conducted in micro/nanofluidic system such as sensing, disease diagnosis, desalination, and energy harvesting, *etc*. In this thesis, target specific binding method for blood cancer is researched and also an efficient type of micro/nanofluidic platform for downstream analysis is proposed.

First, the detection of target blood gene was conducted using ion concentration polarization and target specific binding dCas9 protein. Due to the demands for early stage diagnosis on disease, point-of-care diagnostics for the detection of target gene have been actively studied these days. Among various technologies, PCR is the state-of-art technology used in genomic analysis. But it has critical limitation of high cost, time consuming and simultaneous amplification of error. As an alternative, a method of detecting specific DNA using ion concentration polarization (ICP) phenomenon and changes of the analyte's mobility upon DNA-dCas9 binding has been reported. As a follow up study, this study successfully demonstrated on blood cancer marker (EGFR L858R) at reduced % of target mutation DNA to 1 % (DNA concentration ~ 0.097 nM). We also confirmed that the DNA-dCas9 binding rate was about 25 % which is not have a significant correlation with the target DNA content and detection sensitivity with 1 bp differ off-target. This platform is expected to be utilized as a on/off diagnostic chip for early detection of blood cancer later.

Second, the efficiently designed micro/nanofluidic preconcentrator and online extractor was devised. Among various preconcentration strategies using nanofluidic platforms, a nanoscale electrokinetic phenomenon called ion concentration polarization (ICP) has been extensively utilized due to several advantages such as high preconcentration factor and no need of complex buffer exchange process. However, conventional ICP preconcentrator had difficulties in the recovery of preconcentrated sample and complicated buffer channels. To overcome these, bufferchannel-less radial micro/nanofluidic preconcentrator was developed in this work. Radially arranged microchannel can maximize the micro/nano membrane interface so that the samples were preconcentrated from each microchannel. All of preconcentrated plugs moved toward the center pipette tip and can be easily collected by just pulling out the tip installed at the center reservoir. For a simple and cost-effective fabrication, a commercial printer was used to print the nanoporous membrane as "Nafion-junction device." Various analytes such as polystyrene particle, fluorescent dye, and dsDNA were preconcentrated and extracted with the recovery ratio of 85.5%, 79.0%, and 51.3%, respectively. Furthermore, we used a super inkjet printer to print the silver electrode instead of nanoporous membrane to preconcentrate either type of charged analytes as "printed-electrode device." A Faradaic reaction was used as the main mechanism, and we successfully demonstrated the preconcentration of either negatively or positively charged analytes. The presented bufferchannel-less radial preconcentrator would be utilized as a practical and handy platform for analyzing low-abundant molecules.

Keyword : micro/nanofluidics, ion concentration polarization, target-DNA detection, recovery of preconcentrated sample
Student Number : 2014-22569

Table of Contents

List of Figures

List of Tables

Chapter 1. Introduction

Microfluidics which deals with fluids in the micro scale are widely used and studied from chemistry, biology, to material science. Microfluidics began to be studied intensively by the micro total analysis system (μTAS) proposed in the 1990s and the lab-on-a-chip concept proposed in the late 1990s[1-4]. The main purpose of miniaturization from bulk system to microsystem was to increase analysis performance rather than simply miniaturization. In addition, the microfluidic system offers numerous advantages as followings by reducing its size. A small amount of fluid can be processed in an accurate amount, fast reaction time, easy control of reaction conditions, requiring only a small amount of power. Also, multiplexing is easy so that high throughput can be obtained since it is free from space restrictions compared to bulk system. Therefore, microfluidics continues to expand its application range in a number of fields such as microchemical reaction, liquid biopsy, point-of-care diagnosis, cellomics, drug delivery, bioassay, and tissue engineering, *etc*[1, 5-7].

Through the development of nanotechnology, numerous ways have been developed that can fabricate nanomaterials in a simple way. Thanks to these advances, various phenomena that occur when nanomaterial is grafted into microsystem was able to be investigated[8-11]. In particular, special phenomena occurring on the micro-nano material interface during ion transport are been actively

analyzed and applied to many areas such as sample preconcentration[12-14], desalination[15-17], energy harvesting[18-20], and fluidic transistor[21, 22], *etc*.

This thesis mainly deals with the sample preconcentration systems using ion concentration polarization which is derived by an ion-selective permeable nanomembrane. In the part 2, background for this ion concentration polarization phenomenon is described.

In part 3, nano-electrohydrodynamic direct detection of target blood cancer gene is proposed utilizing ion concentration polarization phenomenon and DNA-capturing phenomenon of dCas9 for liquid biopsy. Liquid biopsy in the cancer diagnosis area has been extensively studied in that it reflects noninvasive, low cost, and tumor-specific information. PCR (Polymerase Chain Reaction) is the most representative method, but error rate is inevitable and base-by-base inspection is time consuming. Recently, dCas9-DNA complex mediated real-time target DNA detection by ion concentration polarization has been reported. Two strategies are utilized for this dCas9 mediated target gene detection method. One is sequence-specific-labeling scheme using mutated Clustered Regularly Interspaced Short Palindromic Repeats associated protein 9 without endonuclease activity (CRISPR/dCas9) and the other is ion concentration polarization (ICP) phenomenon as a mechanism to selectively preconcentrate targeted DNA molecules for rapid and direct detection. It was confirmed that the mutated EGFR (Epidermal Growth Factor Receptor) L858R DNA binds to specific dCas9 so that it can be detected in our methodology. Furthermore, for the possibility of experimental application to clinical

samples in the future, the detection was successfully demonstrated when the ratio of target DNA to total DNA to 1 %. And it was also confirmed that 1 bp recognition is possible.

In part 4, As a method for efficient downstream analysis, preconcentration experiment was conducted in a radially arranged microchannel. The main idea is that when a pipette tip containing the sample is inserted into the center of the device, and positive voltage is applied at the center, the preconcentration occur. Then the solvent flows out toward the rim of each microchannel while target particles are collected in a concentrated volume under the center pipette tip. After the preconcentration step, the user can achieve the collected preconcentrated solution with only pulling out the center pipette tip. To implement the device, a circular nanojunction printing method was devised, and the completed radial preconcentrator device was experimentally demonstrated using 2 μm-size particles, fluorescence dye, and dsDNA. Furthermore, it was confirmed that both positively and negatively charged particles could be preconcentrated in single device by constructing a device which is capable of causing ion concentration polarization through an electrode instead of nanojunction. This was applied to a radial device to build a device for simultaneously preconcentrating in 64 directions. However, since ion depletion occurs by electrochemical reaction, gas, a by-product of reaction continues to be generated. So this type of device could not be applied to long-term preconcentration experiments as the nanojunction device.

In the part 5, the thesis is concluded with the summary and the perspective of these studies.

Chapter 2. Ion-selective Transport Phenomena

2.1. Permselectivity of a Nanoporous Membrane

When the materials containing chemical functional groups encounter with an aqueous solution, functional groups are activated releasing ions and then surface charge is characterized[23]. The magnitude of surface charge density can be defined depending on the ionized functional groups. For example, Glass has SiOH functional group on its surface. When the glass encounters with aqueous solution, H^+ ions are released from the surface forming SiO^- dangling bonds on the glass surface (The charge density of glass surface (σ) ~ -10 x 10^{-3} C/m^2 at pH 7[24]). Then hydrated counter-ions (assume positively charged ions) in aqueous solution (ions that attract molecules in the surrounding solvent) are close to the surface, they are spaced apart from the electrode apart from the surface due to the hydrated molecules. The region where the ions at this distance gather is called outer Helmholtz plane (OHP) layer. Anions absorb even though there are already sufficiently accumulated negative charges inside the Helmholtz plane (specific absorption). And the region where the specific absorbed ions are gathered is called the inner Helmholtz plane (IHP) layer. Outer layer as diffusion. As it goes toward the diffusion layer, the concentration of ions decreases. The Guoy-Chapman-Stern model of the surface-electrolyte interface describes the Stern layer by the inner Helmholtz plane layer and the outer Helmholtz plane layer[25]. The interface of OHP and diffuse layer is referred as the slip plane

4

(or shear plane), and the zeta potential (ψ_z) is defined at this plane. Then electrical double layer is defined throughout these two Helmholtz planes. From the Debye-Huckel approximation,

$$\psi = \psi_z \exp(-\kappa z), \tag{1}$$

the Debye length (λ_D) is defined as the corresponding value of κ which describes the thickness of the electrical double layer.

$$\lambda_D = \kappa^{-1} = \left(\frac{\varepsilon_0 \varepsilon_r k_B \mathrm{T}}{2\mathrm{e}^2 z^2 \mathrm{n}_\infty}\right)^{1/2} \tag{2}$$

where ε_0 is permittivity of free space, ε_r is relative permittivity, k_B is the Boltzmann constant, T is absolute temperature, e is elementary charge, z_i is the valence of ith ion and n_∞ is bulk concentration[26].

In microchannel, the electric double layer is very thin compared to the entire channel, so the electrical influence on the entire microchannel is negligible. But in the case of nanochannel, electrical double layers can overlap each other (The Debye length is 10 nm at KCl 1 mM condition) resulting in a non-zero charge at the center of the channel. These concepts are shown in Figure 2.1. In microchannel (Figure 2.1 (a)), ions can flow along the channel because it is electrically neutral in the bulk and the electric potential is zero. Meanwhile, in nanochannel, the electrical neutral is broken inside the channel and the electric potential has a finite value as the electric double layer overlaps. Therefore, in the nanochannel (Figure 2.1 (b)), permselectivity occurs that selectively allows the passage of counter-ions (positively

5

charged ions in this case). In order to resolve the imbalance of the electric potential inside and outside the nanochannel, an inverse imbalance in ion concentration occurs at each side of nanochannel. This is called Donnan equilibrium[25, 27].
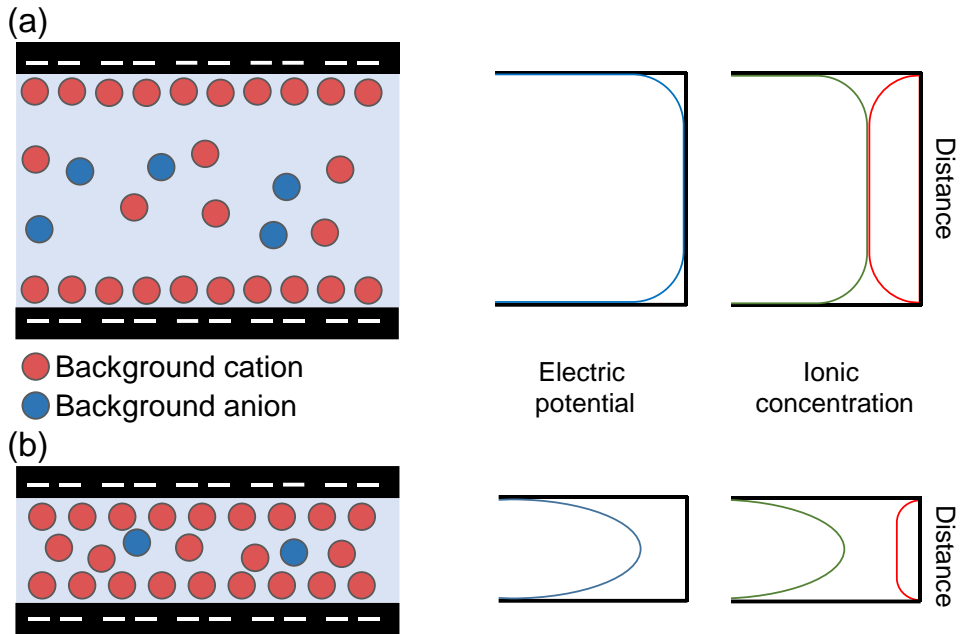
Figure 2.1 (a) In a microchannel, the electrical double layer is typically thin so that the bulk is neutral and the electic potential is zero. (b) In a nanochannel, the electrical double layers typically overlap so that the electric potential has a finite value which prevents co-ions from passing through the nanochannel (modified from R. Karnik, R. Fan, M. Yue, D. Li, P. Yang, and A. Majumdar, *Nano Letters*, 2005, 5(5), 943-948).

2.2. Ion Concentration Polarization

Under electric field along a permselective membrane connecting two separate microchannels, ions are depleted at one edge of the membrane while ions are enriched at the other edge, which is called ion concentration polarization. Nafion membrane is widely used as a permselective membrane. Sulfonic acid functional groups cover the surface of Teflon-based backbone in Nafion membrane. The diameter of nanopores in the membrane is known to be 1 ~ 10 nm and the surface charge density is as high as -500 ~ -200 mC/m^2[28]. Note that the surface charge density of glass is below -13 mC/m^2[24]. The electrical double layers in the nanopores overlap resulting in the Donnan potential inside the pores. Then, only positively-charged ions can pass through the nanopores from anodic side to cathodic side when electric voltage is applied. Remaining negatively-charged ions at the anodic edge of Nafion membrane disperse to satisfy electroneutrality against the membrane. Depletion region where charged species rarely exist appears adjacent to the anodic side of Nafion membrane. Meanwhile, cations passing through the membrane accumulate at the cathodic edge of Nafion membrane so that anions gather toward the Nafion edge to satisfy electroneutrality. This region is called enrichment region where the concentration of ions is particularly high adjacent to the cathodic side of Nafion membrane. The increment of applied voltage results in the decrease of ion concentration at the anodic edge of the membrane. The schematics of ion concentration polarization are shown in Figure 2.2. The state before ion concentration reaches zero at the anodic edge is called the Ohmic regime.

As the applied voltage increases further, there appears ion-depleted region and overlimiting regime begins. It has been known that random vortices grow due to space charge layer in the depletion region.
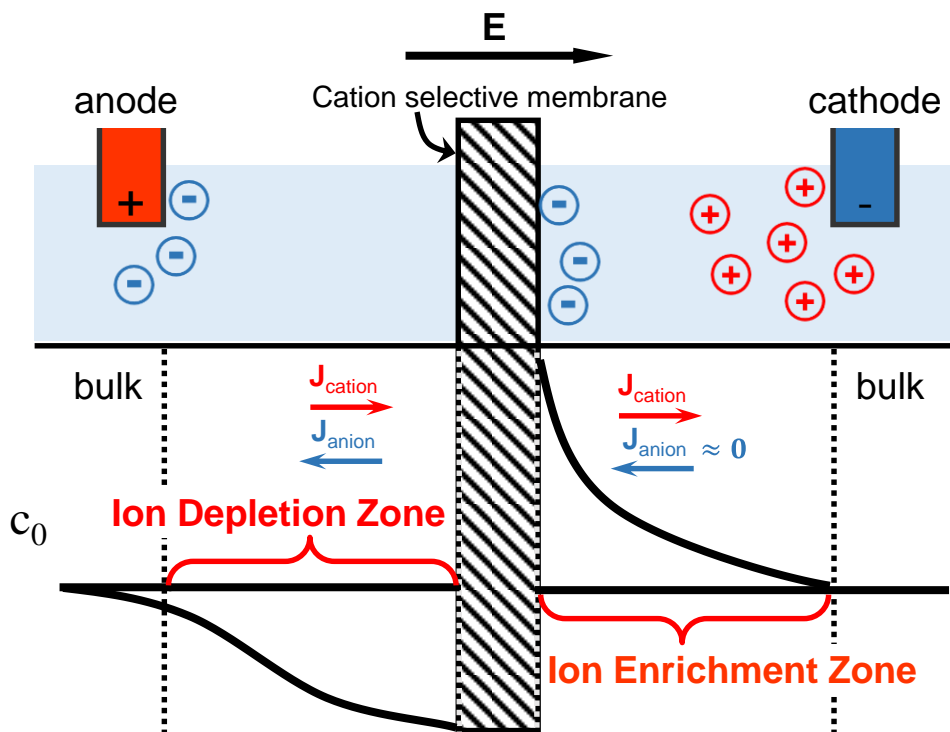
Figure 2.2 Schematic diagram of ion concentration distribution near a cation-selective membrane.

Chapter 3. Detection of target blood cancer mutation using DNA-dCas9 specific binding for liquid biopsy

3.1. Introduction

Liquid biopsy in the cancer diagnosis area has been extensively studied in that it reflects noninvasive, low cost, and tumor-specific information. Also, due to the demands for early stage diagnosis on diseases, point-of-care diagnostics for the detection of target gene have been actively studied these days. Numerous noble technologies such as Sanger sequencing[29], cyclic array sequencing[30], and next generation sequencing (NGS)[31] are being studied to effectively detect target genes in liquid biopsy. By analyzing the floating biosamples in the blood, these state-of-art technologies can provide a variety of detailed information that hardly be provided by invasive tissue-based biopsies[32].

Most of these techniques include polymerase chain reaction (PCR) to amplify infinitesimal amount of information-bearing DNA fragments[33]. Then, electrophoretic separation is required to verify the order of the whole sequence. In general, the electrophoretic resolution between fragments is determined by the difference in electrophoretic mobility, which is determined by the ratio of a fragment`s net charge to the fragment`s friction coefficient. On the other hand, it was impossible to confirm the peak value of the electrophoresis results since there was

almost no difference in mobility for DNA fragments of 50 bp or more DNA due to the free-draining coil structure of it[34-36]. As a method to solve this problem, gel electrophoresis or end-labeled free-solution electrophoresis have been introduced, which can change the mobility of DNA fragments by size[37, 38]. However, these processes are time-consuming and labor-intensive because non-specific labeling and whole sequencing are required. In addition, since the error rate is also amplified during the PCR amplification process[39], diagnostic reliability can be reduced in fields which requires precise diagnosis[40] (*i.e.,* cancer diagnosis).

In order to compensate for the problems in the PCR amplification process, researchers have demonstrated direct nanopore sensing[41-43] and ionic-field-effect-transistor sensor[21, 44]. But these sophisticated methods also have issues such as low signal-to-noise ratio and difficulties in fabrication process. Here, we adopted a sample detection method using ion concentration polarization (ICP) rather than the techniques presented above. Because the electrical double layer is overlapped within the nanojunction[25, 45], only the counter-ion can pass through the nanojunction. This causes an ionic imbalance around the nanojunction, which leads to various physical properties such as depletion layer, locally amplified electric filed in depletion layer[46, 47], non-equilibrium space charge[48-50], electroconvection[51-53], and overlimiting currents[54, 55]. The concentration of charged species in the electrolyte loaded in the micro/nano platform is possible by the ICP phenomenon.

Charged particles can be preconcentrated outside the depletion zone in

microchannels when ion concentration polarization occurs as shown in Figure 3.1 (b). As the voltage was applied, electro-osmosis lets the solution inside the anodic microchannel move from the reservoir. Then, charged molecules in the microchannel are influenced by two different forces: electroosmotic force and electrophoretic force[13, 56-58]. Electroosmotic force is represented as Stokes drag force, $6\pi\mu\mathbf{u}_{EO}R$ where μ is the dynamic viscosity, $\mathbf{u}_{EO}$ is the electroosmotic velocity of bulk which is independent from molecule's properties, and R is the radius of the spherical object. Electrophoretic force can be represented as qE where q is a net electric charge and E is electric field. For negatively charged particles, those two forces are exerted in opposite directions inducing the preconcentration of the particles. On the other hand, the electrophoretic force is significantly different between inside and outside of the depletion zone boundary. This is because the electric field is extremely high inside the depletion zone because there barely exists charged ions. Therefore, due to the electrophoretic force gradient caused by the abrupt difference of electric field, the negatively charged particles are preconcentrated from the outside of the depletion zone boundary. Then, if the concentrated charged species is fluorescently labeled, real-time detection is available. Concentration studies of various biosamples such as DNA[59], protein[12, 60], and cells[61] have been conducted using this ICP induced concentrating mechanism, and a study on target DNA concentration using the specific binding mechanism of dCas9 has been recently reported[62].

Cas9 (Clustered Regularly Interspaced Short Palindromic Repeats associated protein 9 (CRISPR/Cas9)[63]) is a protein whose DNA sequence specificity is

induced by RNA, and is used as a genetic scissors for gene editing technology by binding and cleaving near a specific nucleotide sequence[64]. In previous study, the inactive state of dCas9[65] (catalytically inactive CRISPR associated protein 9) protein was utilized for the experiment since only the characteristic of Cas9 protein binding to a specific nucleotide sequence was required. When RNA-induced dCas9 binds to a specific DNA sequence, electrophoretic mobility is reduced compared to unbound DNA. When the reacted sample is concentrated, different concentration plugs appear due to mobility differences as shown in Figure 3.1 (c), which allows to identify the presence/absence of target DNA. As a follow-up study, in this thesis, we conducted detection using the dCas9 target sequence binding method for EGFR L858R blood cancer DNA, which is the cause of lung cancer. By adjusting the experimental conditions, it was confirmed that the mutated EGFR mutation was successfully detected by suggested method.
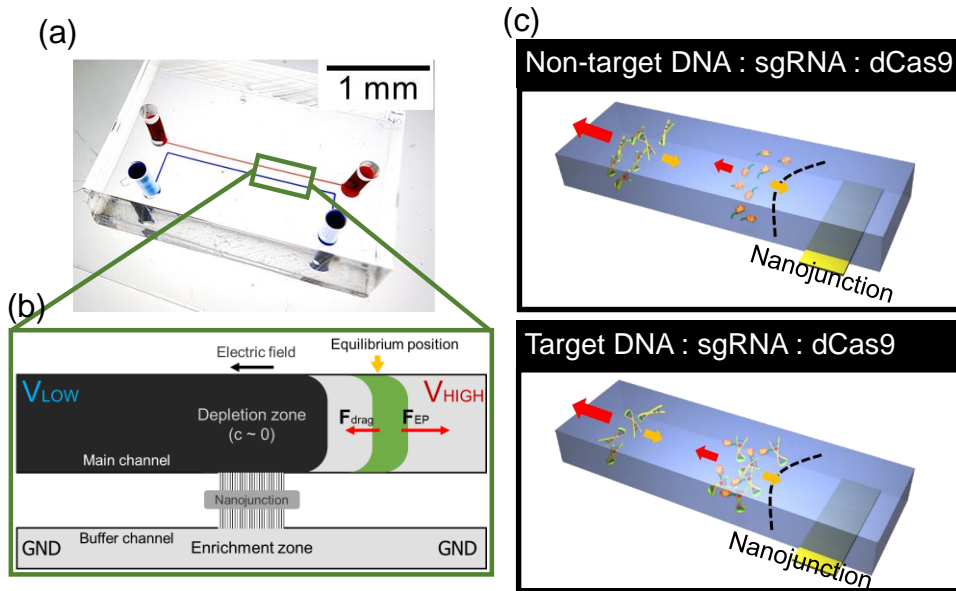
Figure 3.1 (a) Fabricated micro/nanofluidic platform. (b) Schematics of preconcentration of negatively charged sample by ion concentration polarization (c) Schematics of the preconcentration pattern of DNA-sgRNA-dCas9 mixed solution with and without target DNA.

3.2. Experimental methods

3.2.1. Device fabrications

The micro/nanofluidic device consisted of main and buffer microchannels of 15 μm in depth, 150 μm in height and 14 mm in length. The nanojunction made of Nafion was surface patterned as follows. First, a polydimethylsiloxane (PDMS, Sylgard 184 silicone elastomer kit, Dow Corning, USA) fragment that has a straight blank microchannel of 100 μm in width, 5 mm in length, and 50 μm in depth was soft-lithographically fabricated with, and then it was put on a glass substrate to form a blank microchannel. Then, fill the blank microchannel with the Nafion solution (20 wt% resin solution, Sigma Aldrich) by capillary force or negative pressure and detach the PDMS fragment from the glass. After curing the glass at 95 ℃ for 5 minutes, the solidified Nafion resin was remained on the glass substrate, and the depth of the patterned Nafion becomes 1.5 ~ 1.8 μm. This nanojunction has a number of $O(10)$ nm nanopores inside the structure[66]. Simply, it could be thought as a rectangular sponge of 100 μm in width, 5 mm in height, and 1.5 ~ 1.8 μm in depth. If more diluted Nafion resin is used or the depth of blank microchannel is changed, the depth of nanojunction can be adjusted 100 nm ~ 1 μm if necessary. The reasons for the use of Nafion junction are (i) high surface charge of Nafion to obtain high perm-selectivity at physiological electrolyte concentration over 100 mM and (ii) easiness of fabrication as described above. A nanochannel lithographically made of

silicon, glass or PDMS lost its perm-selectivity at an electrolyte concentration over 100 mM due to its thin electrical double layer. Also, Nafion can be easily patterned on a slide glass even at a regular laboratory[18, 67, 68], and this nanojunction fabrication does not require any nano-lithographical facility. After all, another microchannel-patterned PDMS fragment was irreversibly assembled on the surface of Nafion-patterned glass using plasma treatment. This micro/nanofluidic device as shown in Figure 3.1 (a) has been generally employed in a number of literatures for not only biological applications[54, 60, 69] but also fundamental nanoscale research[18, 70, 71].

3.2.2. Materials and Chemical

For the experiment of demonstrating of preconcentration, Alexa 488 (1 µM, Invitrogen, USA) was used as negatively charge analyte. Mcherry dye protein (ex: 587 nm, em: 610 nm) and dCas9 was synthesized by self-aligning process to form a synthetic protein. dCas9 and sgRNAs were synthesized by in vitro transcription using T7 RNA polymerase. Targeted DNA molecules were synthesized by introducing the EGFR L858R gene sequence into plasmid followed by PCR. In the process of PCR to produce DNA targets, we used 3' FAM labeled primers (ex: 494, em: 518) to obtain fluorescence labeled DNA molecules (Macrogen, South Korea). All biosamples preparation were conducted as courtesy of Dr. Jina Yang.

3.2.3. Experimental apparatus

An external voltage was applied using two source measurement unit (SMU 238, Keithley, USA) though Pt electrodes. They shared the common ground and V_{HIGH} and V_{LOW} were applied from each SMU to the reservoirs (anode to main microchannel and cathode to buffer microchannel). An inverted fluorescence microscope (IX-51, Olympus, Japan) and a CCD camera (DP73, Olympus, Japan) were used to detect and trace the fluorescence-labeled samples. Commercial software (CellSense, Olympus, Japan) was used to synchronize the CCD camera with the microscope and to analyte the images.

3.3. Results and discussions

3.3.1. Concentrating rate comparison through florescence dye

In general, the flux of a negatively charge analyte derived from the Nernst-Planck equation in the x-direction is expressed as

$$j_A = -D_A \frac{dc_A}{dx} - \mu_A c_A E_x + c_A u_x \tag{3}$$

Where j_A is the area-averaging analyte flux, D_A is the analyte diffusivity, c_A is the analyte concentration, E_x is the area-averaging electric filed, u_x is the flow-filed in x-direction, and μ_A is the electrophoretic mobility of analyte. If diffusive transport is minor in the microchannel, the concentrating behaviors of the analyte are determined by the scale difference between electrophoretic migration and convective transport. When the force of electrophoretic migration is larger than that of convective transport, the plug of the preconcentrated analyte is consistently moved toward the bulk reservoir. In order to check whether the concentration ratio required for blood cancer diagnosis can be obtained by this propagating preconcentration, demonstration was conducted using Alexa 488 fluorescence dye. Assuming that diffusive transport in the microchannel is minor and that all analytes injected from the bulk reservoir are preconcentrated, the flux of negatively charge analyte can be approximated as $j_{A0} = -\mu_A c_{A0} E_0 + c_{A0} Q$, where j_{A0} is the influx of analyte from bulk reservoir, c_{A0} is the bulk concentration of analyte, E_0 is the magnitude of the electric filed across the main microchannel, and Q is the flow rate. For easy fluorescence

image analysis, bulk concentration of Alexa 488 dye was prepared to 1 μM. V_{LOW} was fixed at 5 V and the experiment was conducted by changing V_{HIGH} to 20, 40, and 70 V. At this time, substituting the mobility of Alexa 488 (3.61 x 10^{-8} m²/V/s[72]), the influx of Alexa dye at 20 V, 40 V, and 70 V voltage conditions (V_{HIGH}) were calculated as 6.230 x 10^{-17} mol/s, 12.82 x 10^{-17} mol/s, and 18.23 x 10^{-17} mol/s, respectively. When the size of preconcentration volume unit was defined as 150 μm width x 100 μm length x 15 μm depth, these values corresponded with the concentrating rate of 16.79 μM/min, 34.18 μM/min, and 48.60 μM/min, respectively. Comparing the calculated values with the experimental results, for each voltage conditions, the Alexa concentration over time was obtained as shown in Figure 3.2. The calculated values were expressed as dotted line and the values obtained through the experiment were express as solid line. In the 20 V condition (V_{HIGH}), it was confirmed that the calculated value and the experimental value were almost identical to the dye concentration with time. In the 40 V condition (V_{HIGH}), It was confirmed that the dye was concentrated about 100-fold within 3 minutes under our experimental conditions. The dye concentration was saturated after about 3 minutes, because as the concentration of the plug consistently increased and thickened, diffusion occurred from the central point of preconcentration to the outside[73], and it was not possible to include all the preconcentrated analytes in the set unit volume. In the 70 V condition (V_{HIGH}), saturation proceeded within about 2 minutes, making it difficult to compare the concentration calculated values and experimental values.

Then, by calculating the mobility of the dCas9-sgRNA-DNA complex in the same
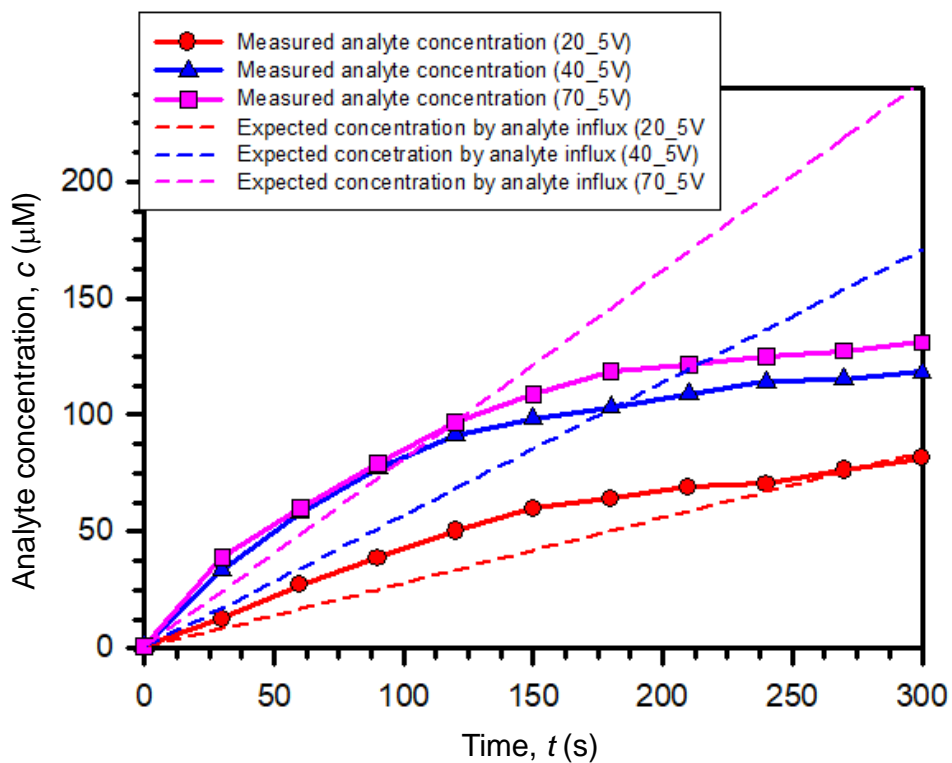
Figure 3.2 concentrating rate of fluorescence dye (1 μM, Alexa 488) by changing the V_{HIGH} conditions (20 V, 40 V, and 70 V) while V_{LOW} was fixed at 5 V. experimental results are indicated by solid line and calculated values are indicated by dotted line.

2 1

way as Alexa dye, we tried to calculate the sample concentrating rate according to the applied voltage versus the initial DNA concentration. If the initial DNA concentration was set to 100 pM and the electrophoretic mobility of 100 bp DNA-sgRNA-dCas9 complex (2.62×10^{-8} m^2/V/s[62]) was substituted, DNA influx under 20 V, 40 V, and 70 V (V_{HIGH}) condition was calculated as 8.68×10^{-21} mol/s, 1.84×10^{-20} mol/s, and 2.86×10^{-20} mol/s, respectively. Corresponding with the unit area (150 μm x 100 μm x 15 μm), the concentrating rate was calculated as 2.32 nM/min, 4.90 nM/min, and 7.62 nM/min, respectively. Compared with the known optically detectable level of 10 nM[59], the experiment was conducted with the expectation that the preconcentration plug could be observed within 3 minutes and 2minutes respectively under 40 V conditions and 70 V conditions (V_{HIGH}) for 100 pM of DNA samples. The evaluated parameters used in calculation are shown in Table 3.1.

Alexa 488			
Applied voltage	**20_5V**	**40_5V**	**70_5V**
c_A (mol/m^3)	0.001		
μ_A (m^2/V/s)	3.61x10^{-8}		
V^* (m^3)	2.25x10^{-13}		
|**E**| (Vm)	2.41x10^{-6}	5.62x10^{-6}	1.04x10^{-5}
Q (m^3/s)	1.50x10^{-13}	3.31x10^{-13}	5.59x10^{-13}
Influx/V^* (μM/min)	16.79	34.18	48.60
EGFR L858R mutation DNA			
Applied voltage	**20_5V**	**40_5V**	**70_5V**
c_A (mol/m^3)	10^{-7}		
μ_A (m^2/V/s)	2.62x10^{-8}		
V^* (m^3)	2.25x10^{-13}		
|**E**| (Vm)	2.41x10^{-6}	5.62x10^{-6}	1.04x10^{-5}
Q (m^3/s)	1.50x10^{-13}	3.31x10^{-13}	5.59x10^{-13}
Influx/V^* (nM/min)	2.316	4.90	7.62

Table 3.1 Parameter values of Alexa 488 and DNA used to calculate the concentrating rate. The initial concentration of Alexa and DNA was set to be 1 μM and 100 pM, respectively.

3.3.2. Electrokinetic behavior of on/off-target DNA with dCas9

Experiments as shown in Figure 3.3 were performed to confirm that EGFR mutation DNA can be specifically detected using the RNA guided dCas9 DNA binding method. For the binding of dCas9-sgRNA to targeted DNA, dCas9 (1.07 μM), sgRNA (15 μM) were firstly mixed in a reaction buffer solution (3 μL, 100 mM NaCl, 20 mM Tris-HCl, 5 mM MgCl$_2$, 5 % glycerol, pH 7.5) and incubated at 37 °C for 15 minutes. Then, after resting at room temperature for 1 minute, DNA (194 nM) was mixed to prepare 15 μL, 1 X reaction solution, and incubated again at 37 °C for 30 minutes. After the entire reaction, the final solution was prepared by diluting the fully reacted solution one twentieth in RNase free water (final concentration of DNA was 9.72 nM, which was 4.16 pmol in 300 μL final solution). In Figure 3.3 (a), FAM dye-labeled free DNA (EGFR mutation) concentrating experiment was conducted. Since the absence of mcherry-labeled dCas9, preconcentration plug was observed only in the green filter. Meanwhile, mcherry-labeled RNA-dCas9 sample concentrating experiment is shown in Figure 3.3 (b) In this case, since FAM dye-labeled DNA was not contained in the sample, preconcentration plug was observed only in the red filter. Since the electrophoretic mobility of dCas9 (1.09 x 10^{-8} m^2/V/s[62]) is lower than that of free DNA (3.67 x 10^{-8} m^2/V/s[36]), it was confirmed that the progress of the preconcentration plug in the dCas9-sgRNA experiment was slower. Figure 3.3 (c) shows the experimental result of sample mixed with EGFR wild type, sgRNA, and dCas9. Since dCas9-sgRNA was designed to target and bind to the EGFR mutation, dCas9-sgRNA was

not bound to EGFR wild type DNA, and there was no mobility-shift of DNA. Then a preconcentration plug concentrating at the same position as free DNA in the green filter and a preconcentration plug concentrating at the same position as dCas9-sgRNA in the red filter were observed. The most important result of sample mixed with EGFR mutation, sgRNA, and dCas9 is shown in Figure 3.3 (d). The specific binding of dCas9-sgRNA to free DNA altered the electrophoretic mobility to 2.62 x 10^{-8} m^2/V/s so that two preconcentration plugs were observed in the green filter and a one preconcentration plug was observed in the red filter, which was at the same position as the following plug in the green filter. The following plug was slower than free DNA plug and formed at a preceding position of the dCas9-sgRNA plug. Through the above experiment, it was confirmed that dCas9 associated gene detection can be useful for single base pair mismatch mutations. However, it is necessary to check the dCas9 binding response for various blood cancer mutations, as previous studies have shown that the specific DNA binding rate of dCas9 decreases rapidly as the single mismatch is further away from the PAM site[50, 71, 74].
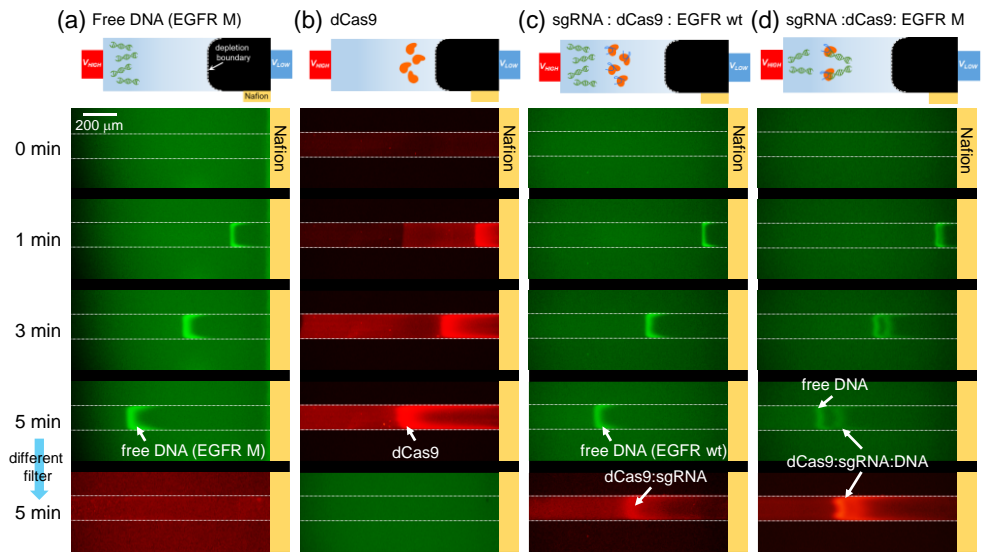
Figure 3.3 Electrokinetic behaviors of (a) free DNA, (b) dCas9, (c) sgRNA:dCas9:EGFR wild type DNA and (d) sgRNA:dCas9:EGFR mutation DNA. The electrophoretic mobilities of free DNA, dCas9, and sgRNA:dCas9:EGFR mutation were calculated as 3.67 x 10^{-8} m^2/V/s, 1.09 x 10^{-8} m^2/V/s, and 2.62 x 10^{-8} m^2/V/s, respectively.

3.3.3. Detection sensitivity depending on the ratio of target gene

In an actual clinical environment, the fragment including the target mutation sequence is infinitesimal compared to the total amount of human chromosome[75-78]. Considering this, the dCas9-sgRNA binding test was performed while adjusting the ratio of target EGFR mutation DNA. To verify that dCas9-sgRNA conducted target specific binding, DNA composition was carried out with FAM dye-labeled EGFR mutation DNA and non-FAM dye-labeled JAK2 wild type DNA. At this time, the total number of moles of DNA participating in the reaction was maintained (4.16 pmol in final solution) matched as the previous section experiment. Figure shows the experimental results of off-target mixed samples. A voltage of 40 V (V_{HIGH}) was applied to the sample in which EGFR mutation and JAK2 wild type were mixed in a ratio of 50:50 (concentration of target (c_{target})= 4.86 nM) as shown in Figure 3.4 (a). According to the experimental result after 2 minutes, two preconcentration plugs were observed in the green filter, and it was confirmed that the position of the following plug and the position of the dCas9-sgRNA preconcentration plug in the red filter were the same. This indicated that sequence specific binding occurred successfully in the mixed sample condition. In addition, the experiment was carried out by changing the mixing ratio of EGFR mutation and JAK2 wild type to 10:90 (c_{target} = 0.972 nM, Figure 3.4 (b)), 5:95 (c_{target} = 0.486 nM, Figure 3.4 (c)), and 1:99 (c_{target} = 0.097 nM, Figure 3.4 (d)), and since the fluorescence signal of dCas9-sgRNA-DNA preconcentration plug was too weak under 40 V (V_{HIGH}) condition, 70 V (V_{HIGH}) was applied at the system. As in the 50:50 case, the position of the

following preconcentration plug in the green filter matched the position of the preconcentration plug in the red filter. This proved that target specific binding occurred properly with our method even when the total sample contains only 1 % of the target DNA. It is known that when artificial sequencing is conducted in blood plasma of real sample, DNA molecules are generally fragmented into 100 to 150 bp[79]. Among these, if the ratio of the fragment containing the actual target blood cancer mutation is calculated as mutation ratio*100 bp/human chromosome, the goal was set to detect about 0.1 % of the total sample. This is expected to be achieved through optimization such as conducting an effective refining process or finding the optimum voltage-flow rate that can maximize the concentration ratio. By analyzing the fluorescence intensity from the preconcentration result on the green filter shown in Figure 3.4, the binding rate of dCas9-sgRNA and target DNA was able to be calculated. Using the imageJ analysis tool, the fluorescence intensity of the preconcentration plug compared to the distance from Nafion was obtained. The result of analysis along the x-axis was approximated by a quadratic function, and integral was performed on the location of the plug, and the result of analysis along the y-axis was averaged. By multiplying these two results, the total fluorescence intensity for each plug was obtained (fluorescence intensity of leading preconcentration plug: fp_1, fluorescence intensity of following preconcentration plug: fp_2). Then, the specific target binding rate was obtained by $fp_2/(fp_1+fp_2)$ resulting in 25.91 % of binding rate, averagely. It was found that this result was not significantly affected by the target DNA ratio in the total sample.
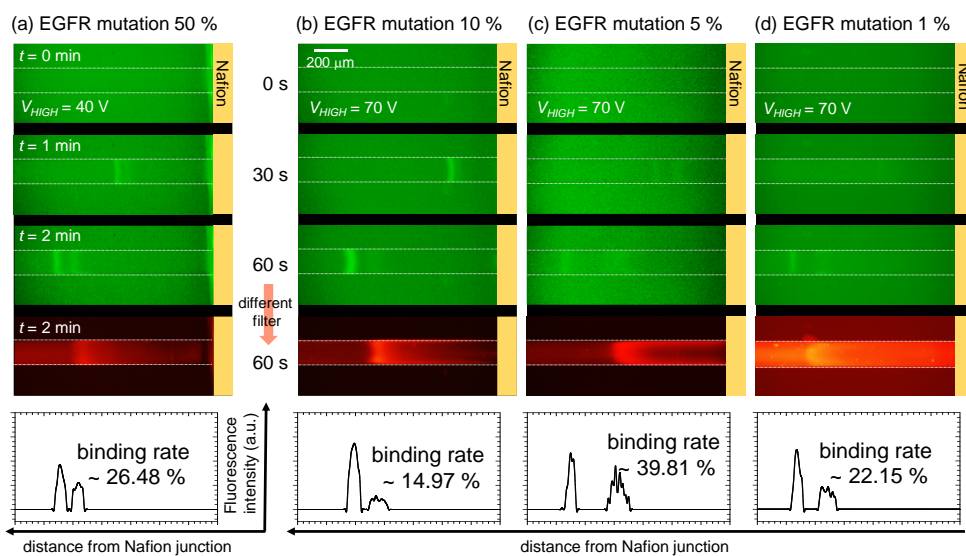
Figure 3.4 Preconcentration tests according to target DNA ratio (off-target: JAK2 wild type DNA). The fluorescence intensity was a function of distance from the Nafion. The binding rated obtained through the analyzed graphs were (a) 26.48 % - EGFR mutation 50 %, (b) 14.97 % - EGFR mutation 10 %, (c) 39.81 % - EGFR mutation 5 % and (d) 22.15 % - EGFR mutation 1 %. 40 V (V_{HIGH}) was applied at (a) while 70 V (V_{HIGH}) was applied at (b)-(d).

3.3.4. Detection sensitivity with 1 bp differ off-target

Conventionally, gene editing technologies that recognize and cut a specific nucleotide sequence in DNA include zing finger nuclease (ZFN) and transcription activator-like effectro nuclease (TALEN). Furthermore, CRISPR/Cas-derived RNA-guided endonuclease (RGEN) using Cas9 is the most recently developed technology. RGEN technology induces DNA sequence specificity by RNA. It recognized the protospacer adjacent motif (PAM) nucleotide sequence immediately after the 20 bp nucleotide sequence corresponding to the spacer and specifically binds 3 bp therefrom[68-71]. The following work was conducted to more rigorously verify that the dCas9-sgRNA specific binding technology is well applied and can be preconcentrated in the ICP platform. Then, the off-target DNA was replaced from JAK2 wild type to EGFR wild type as shown in Figure 3.5 (a), (b). When EGFR mutation is mutated, one base pair is mutated to form a PAM (NGG) sequence[80, 81], which enables dCas9-sgRNA to specifically bind to EGFR mutation. Therefore, sequence of JAK2 wild type is completely different from that of EGFR mutation, while EGFR wild type and EGFR mutation differ in only one base pair. The number of moles of total DNA was also adjusted to 4.16 pmol as previous experiments, and target EGFR mutation was labeled with FAM dye while off-target EGFR wild type was not labeled with FAM dye. The ratio of target EGFR mutation and off-target EGFR wild type was mixed as 5:95 (c_{target} = 0.486 nM, figure), 1:99 (c_{target} = 0.097 nM, figure), and 70 V (V_{HIGH}) was applied over the system. Two preconcentration plugs was observed in the green filter, and the position of the following

preconcentration plug coincided with that of plug observed in the red filter. Through this, it was verified that dCas9-sgRNA sequence specific binding was able to distinguish even one base pair difference. In addition, an off-target (FAM-labeled EGFR wild type 5 %, non-FAM-labeled JAK2 wild type 95 %) was also preconcentrated in 70 V (V_{HIGH}) applied condition to verify whether the total amount of concentrating rate was preserved in the presence of the target DNA and in the absence of target DNA as shown in Figure 3.5 (c). fluorescence intensity of preconcentration plugs were analyzed in the same way as in the previous section. The calculated total plugs fluorescence intensity of three samples (EGFR mutation 5 % + JAK2 wild type 95 %, EGFR mutation 5% + EGFR wild type 95 %, and EGFR wt mutation 5 % + JAK2 wild type 95 %) are 7170.47, 6959.92, and 6078.15, respectively. For accurate calculation, the background intensity value was adjusted. As depicted above, the preconcentration position is determined by the force balance between electrophoretic force and convective force. As the convective force affects equally on the whole system, the leading plug receives a larger force toward the bulk reservoir by electrophoretic force compared to following plug. Then, substituting the above calculation result, it is assumed that as the leading plug received larger electrophoretic drag force so that the plug accumulation for plug maintenance was slightly weakened.
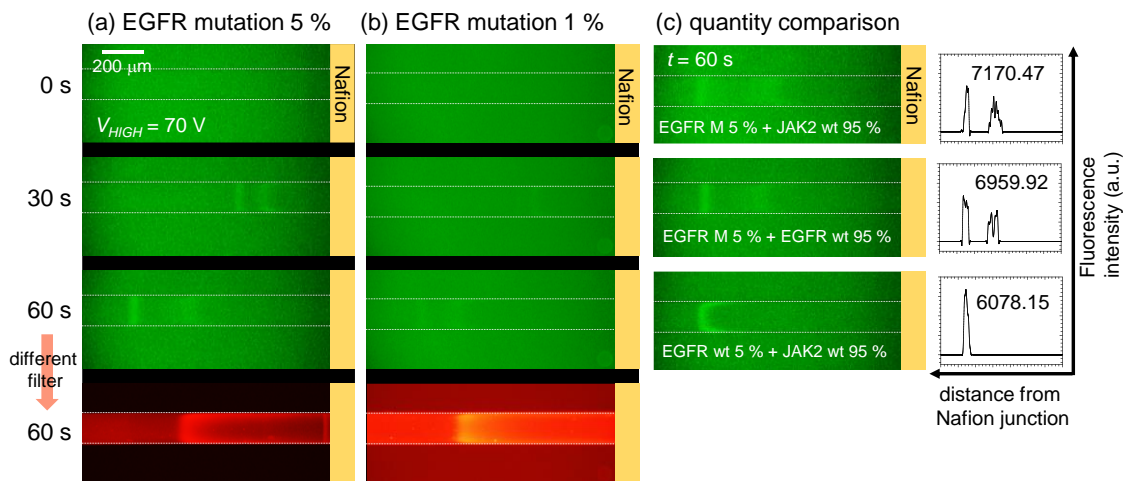
Figure 3.5 Identification tests when on-target and off-target differ by 1 bp. (a) EGFR mutation 5 % + EGFR wild type 95 % (b) EGFR mutation 1 % + EGFR wild type 95 % (c) Concentration fluorescence analysis according to the type of off-targets.

3.4. Conclusions

The demand for rapid and accurate liquid biopsy diagnosis in the field of blood caner, viruses, cytology continues to increase. By using the noble property that dCas9-sgRNA binds to a specific nucleotide sequence and changes the electrophoretic mobility of the analyte, we succeeded in detecting low concentration (~ 100 pM) of target blood cancer DNA without PCR process. When a sample containing target DNA was loaded on a micro/nanofluidic platform and voltage was applied, the sample was preconcentrated by the ICP phenomenon. At this time, two preconcentration plugs of DNA bound to dCas9-sgRNA and unbound DNA were observed by the difference in electrophoretic mobility. Since the electrophoretic mobility of dCas9-sgRNA is lower than that of 100 bp free DNA, when the two were combined, the progress of the preconcentration plug was slower than that of free DNA. The concentrating rate of the analyte was confirmed under a specific voltage conditions (20 V, 40 V, and 70 V (V_{HIGH}) while V_{LOW} was fixed as 5 V) using a fluorescent dye, and it was expected that it would be possible to concentrate a sample at ~O(pM) level to an optically detectable level within few minutes. In experimental demonstrations, 100 bp of EGFR L858R DNA was adopted which is the cause of lung cancer and we successfully confirmed that specific binding of dCas9-sgRNA binding was able to be detected by our methodology with the binding ratio of about 25 %. It was also verified that the detection method was effective even when only 1 % of the target DNA was included in total sample.

However, in the case of real samples in clinical practice, there exists many limiting

conditions so that it is challenging to detect target DNA with this platform. Real sample DNA molecules obtained from clinic should be labeled with an intercalating dye such as YOYO or TOTO. Since these dyes have their own electrophoretic mobility, when labeled with DNA, there may be less difference in the speed of the preconcentration plug between free DNA and dCas9-sgRNA-DNA. By adjusting the Q and E of the system, plugs with larger electrophoretic mobility can be adjusted to proceed slower while plugs with smaller electrophoretic mobility can be adjusted to proceed faster. In addition, after fragmentation, the refining process is necessary because the ratio of fragments containing the target gene to the whole human chromosome is very low (0.1 % or less). When compared with our experimental conditions, there are methods such as concentrating at a 1 X PBS background electrolyte or close to it for less dilution and grafting a sample extracting device with our system. There have been several attempts to concentrate bio samples under 1 X PBS background using ICP phenomenon[41]. Implementing an optimal system in consideration of high background concentration conditions, extraction device, and labeling intercalating dye on DNA, it is expected that the dCa9-mediated target DNA detection platform using ICP will be able to provide a rapid and effective method for the area of blood cancer liquid biopsy.

Chapter 4. Nanoelectrokinetic bufferchannel-less radial preconcentrator and online extractor by tunable ion depletion layer

4.1. Introduction

Since a preconcentration is an essential step for sensing various low-abundant analytes in bio- and environmental- applications[3, 4, 82], a number of mechanical mechanisms such as membrane filtration[83-85], inertial focusing[86], acoustophoresis[87], and thermophoresis[88, 89], *etc*. have been actively investigated. More recently, due to the easiness of electrical operations, electrokinetic techniques such as isotachophoresis[90, 91] and field amplified stacking[92-96], *etc*. have been competitively reported using micro/nanofluidic platform. Among the technologies, a nanoscale electrokinetics phenomenon called ion concentration polarization (ICP) mechanism has extensively utilized recently, due to several critical advantages of high preconcentration factor (most of target analytes from infinite volume of reservoir would be stacked at specific locations inside a microchannel) and no need of complex buffer exchange processes[54, 97-105]. ICP is the electrochemical phenomenon that observed at the interface of the nanoporous membrane and electrolyte solution[16, 18, 67, 106-111]. When a dc voltage bias is applied to the micro/nano hybridized platform which contains

electrolyte, the imbalance of ions occurs at both ends of the nanoporous membrane due to the ion selective permeability of the membrane. To balance electro-neutrality, extended space charge (ESC) layer was formed adjacent to the electrical double layer[112-115]. Inside ESC layer, the concentration of cation is higher than one of anion. This is the typical process of balancing cation and anion in ICP phenomenon rather than water splitting or metal oxidation. In case of the cation-selective membrane, an ion depletion zone appears at the anodic side of the membrane and an ion enrichment zone appears at the cathodic side of the membrane. Then the charged molecules in the electrolyte are preconcentrated at the boundary of the ion depletion zone by the force balance between convective drag force and electrophoretic migration in the microchannel[54, 57, 97, 116]. While one can achieve high preconcentration factor over a million fold by ICP[98], it is extremely difficult to recover the preconcentrated plug in the microchannel because the concentration gradient of the preconcentrated plug to the depletion zone is so large that it dissipates momentarily when the voltage bias is turned off for extracting the plug. To overcome this problem, several studies have been conducted to use preconcentrated plug *in-situ* such as confining the preconcentrated plug in the oil phase in combination with the droplet generator[117] or immobilizing functionalized beads at the microchannel bottom where the target molecules were preconcentrated for immunoassay[12, 118, 119]. However, a simple extraction method without losing the useful preconcentration factor should be still required for downstream analysis.

While two microchannels connected with a nanoporous membrane has been

served as a basic platform of the ICP preconcentrator[54, 120], a simple straight microchannel with nanoporous membrane only at the bottom of microchannel has reported to realize the ICP preconcentrator as well[119, 121, 122]. We had reported this concept for the first time and this simple device can minimize the unnecessary electrical connections while keeping the similar preconcentration factor so that it would provide more commercializable platform[119]. Eliminating buffer microchannel would greatly save the space so that it provides beneficial freedom for the high degree of multiplexing or radial design. For further enhancement of throughput and easiness of sample recovery, we have invented a radial type microchannel network on 2010 to maximize the microchannel/nano membrane interface which results in significantly improved throughput[123]. However, this patent was abandoned recently because the bufferchannel-less concept in this patent (Nafion on top of electrode) was hard to be realized, and we have been keeping develop a different bufferchannel-less concept, which is the new bufferchannel-less concept in this work (straight microchannel with Nafion at the bottom of microchannel). Using this radial concentrator, not only the throughput but also electrokinetic stability[124-130] can be enhanced. Radial configuration confined the preconcentrated sample in each microchannel and, thus, the effective length scale can be discretized[47, 108, 130-134]. In such micro-confined environment, undesirable electrokinetic instability can be largely suppressed. Furthermore, the preconcentrated plugs in each radial microchannel receded toward the center so that one can easily extract the whole plugs using a conventional pipette tip at the center.

The dynamics of preconcentrated sample are categorized into two behaviors[62]. If the plug was pinned near the nanojunction, it is called "stacking behavior". If the plug is receded from the nanojunction which is the case of this work, it is called "propagating behavior". Thus, the plugs of local extremely high concentration in front of each ion depletion zone can be collected at the center, meaning we fully utilized the advantages of ICP preconcentrator. For example, 50 uL of sample solution can be 5 uL of preconcentrated sample solution at the center which is enough volume for downstream chip-to-world analysis. This type of ICP device was named as "a bufferchannel-less radial preconcentrator and online extractor". Few other radially structured preconcentrator had already been reported[135, 136] but their basic layout was traditional main microchannel-membrane-buffer microchannel connection so that it could collect the analytes only inside the radially positioned microchannel itself.

In this work, our bufferchannel-less radial preconcentrator can preconcentrate the whole analytes in the inserted pipette tip so that one can achieve both reasonably useful preconcentration factor and easy sample recovery for a direct downstream analysis. Here we successfully demonstrated that microbead, fluorescent dyes, and dsDNA were preconcentrated and easily extracted. Moreover, since Nafion based preconcentrator mainly works on negatively charged molecules, silver electrode was printed instead of Nafion for the more general applicable preconcentrator. With printed electrode preconcentrator, the ion depletion zone was generated using the Faradaic reaction[137, 138] as the main mechanism and the negatively charged

molecules as well as the positively charged molecules were successfully preconcentrated in this bufferchannel-less radial type device. Therefore, this device is greatly useful lab on a chip platform for most of sample preparation step in bio-chemical-analysis. Preconcentrating low abundant molecules at reasonably high amplification factor and easy extraction of preconcentrated sample would have significant commercial capability.

4.2. Experimental methods

4.2.1. Device design

In this work, two types of device were demonstrated. The major difference between them was the way they mediated the ion depletion zone. ICP was used to mediate ion depletion zone using nanoporous membrane called as "Nafion-junction device", and Faradic reaction was employed using printed silver electrode called as "printed-electrode device". Both types have the same operation procedures, and the step-by-step operation procedures were shown in Figure 4.1. Buffer solution without analytes was injected into the microchannel by pressure in advance. Then, step (i) was injecting a commercial pipette tip which contained sample solution at the center of each device. Step (ii) is sample loading and preconcentration by applying electric field between the radial electrode and the pipette tip. The polarity of dc electric field was determined by the target analytes, *i.e.* positive at center and ground at the electrode for negatively charged analytes and *vice versa*. Then solvent in the pipette tip flowed out toward the rims by electro-osmotic flow and pressure driven flow. Because the depletion zones at each microchannels converged toward the center pipette tip, it prevented the target analytes from flushed outward and all of analytes in the pipette tip were sieved by the depletion boundary, leading high preconcentration factor. Step (iii) is the recovery of the analytes. After removing the solution from all the rims, the pipette tip containing preconcentrated analytes with minimum amount of solvent was pulled out for easy recovery of the analytes. It was expected that the preconcentration and recovery efficiency could be easily increased

by changing the number of branch channels of the device or duration time of preconcentration, *etc*. A fabricated 16 branch channel device with Nafion and 64 branch channel device with printed electrode were also shown in Figure 4.1. For the Nafion-junction device and printed-electrode device, each microchannel had the dimension of 100 μm width × 50 μm depth × 7 mm length and the dimension of 50 μm width × 50 μm depth × 7 mm length, respectively. In order to operate ICP at stable condition, the characteristic length scale should be around O(10) μm as previous literatures suggested[18, 131]. We have tested 75 μm height device, but the results were extremely unstable. This is the consideration for choosing 50 μm height.
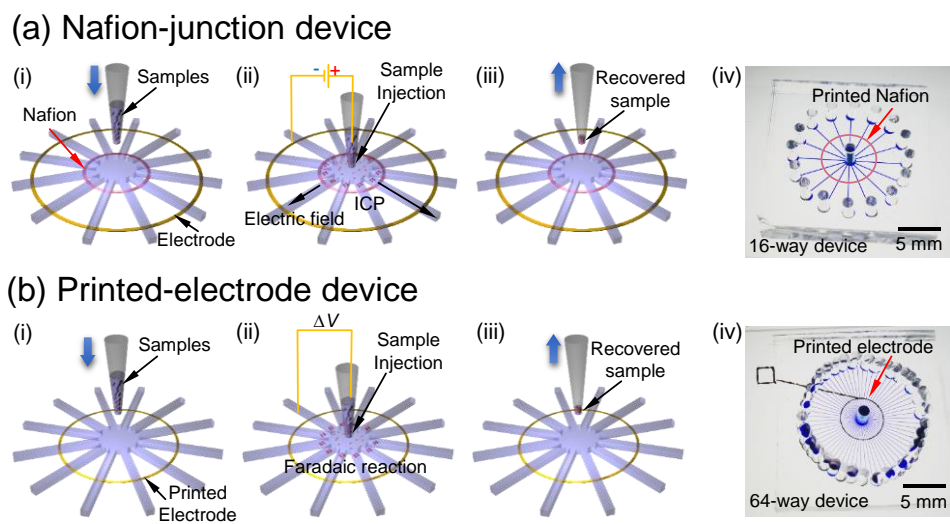
Figure 4.1 Schematics of operation procedures and device pictures of (a) Nafion-junction device and (b) printed-electrode device. Both devices had the same operation procedures. (i) Buffer injection and preparation of the sample solution, (ii) sample injection and preconcentration of molecules, (iii) extraction and recovery of preconcentrated molecules, and (iv) photo of fabricated device.

4.2.2. Device fabrication

The SU8 microchannel mold was fabricated on the silicon wafer by photoresist fabrication method. To replicate the microchannel mold on the polydimethylsiloxane (PDMS, Sylgard 184 Silicon elastomer kit, Dow Corning, USA), a PDMS precursor solution (the mixture of pre-polymer and curing agent at the ratio of 10:1) was poured on the silicon wafer which had microchannel mold, and cured in an oven at 75 ℃ for 4 hours. For the Nafion-junction device, Nafion® resin solution (wt 20%, Sigma-Aldrich, USA) was used as a cation perm-selective membrane. Nafion printing method was used to pattern atypical shape of nanoporous membrane on the glass using commercial inkjet printer (EPSON, K-100, Japan). A detailed method for Nafion printing is described in Appendix A. Nafion was diluted by DI water at the ratio of 1:7 for matching the viscosity of commercial ink as shown in the Table 1. On the commercial inkjet printer, diluted Nafion and glass was used instead of commercial ink and printing paper, respectively and then, Nafion was simply printed on glass. Finally, printed Nafion was heated on the hot plate at 95 ℃ to remove solvent from Nafion solution, remaining only solid Nafion solute on the glass.

For the printed-electrode device, silver ink (Silverjet DGP 40LT-15C, Advanced Nano Products, USA) was circularly printed on the glass by a super inkjet printer (SIJ-S030, SIJ Technology, Inc., Japan). Printed silver electrode was heated on the hot plate at 130 ℃ for 2 hours to have 11 $\mu\Omega$·cm of electrical resistivity. Then, PDMS mold with microchannels was bonded with the Nafion patterned (or electrode printed) glass by O_2 plasma treatment (FemtoSience, CUTE-MP, Korea) and cured on the hot

plate at 95 °C for 2 hours.

4.2.3. Materials

For the Nafion-junction device, the mixture of 1 mM potassium chloride (Sigma Aldrich, USA) and fluospheres polystyrene (1 μm, blue-green (430/465) particle, Invitrogen, USA), the mixture of 1 mM potassium chloride and Alexa fluorescent dye (Alexa 488, (200 nM, Invitrogen, USA) solution, and 947 bp length of A260 double stranded DNA (Oligonucleotides were customized by Macrogen Inc., Korea) with 0.1 X Phosphate-Buffered Saline buffer (Sigma Aldrich, USA) were used. For the printed-electrode device experiment, the 1 mM Tris-HCl (pH 5.6) solution was prepared by mixture of tris(hydroxymethyl) aminomethane (Tris base, Sigma-Aldrich, USA) and hydrochloric acid as a buffer and sulforhodamine B (SRB), (50 nM, Sigma Aldrich, USA) was used as a negatively charged dye while rhodamine 6G (50 μM, Sigma Aldrich, USA) was used as a positively charged dye.

4.2.4. Experimental Setup

Viscosity of DI water, commercial ink, and diluted Nafion was measured by viscometer (SV-10, A&D, Japan). An electrical voltage was applied by source measure unit (Keithley 236, USA) through Ag/AgCl electrode. The behaviors of analytes were traced by an inverted fluorescent microscope (IX-53, Olympus, Japan)

and analyzed by ImageJ, CellSense and   spectrophotometer for dsDNA experiment
(Qiagen, Germany).

4.3. Results and discussions

As previously stated, experiments were conducted on two types of devices (Nafion-junction device and printed-electrode device). First, Nafion-junction device was demonstrated with preconcentration and extraction of microparticles, fluorescent dye, and dsDNA and then printed-electrode device was demonstrated with preconcentration of either positively or negatively charged fluorescent dyes.

4.3.1. Nafion-junction device

4.3.1.1. Polystyrene microparticle demonstration

To demonstrate the feasibility of bufferchannel-less radial preconcentrator, the preconcentration of 1 μm-size polystyrene microparticle at 1 mM potassium chloride buffer background solution was firstly operated in the 8-way radial preconcentrator and the fluid motion of microparticles were visualized as shown in Figure 4.2 (a). The image was taken from only 2 channels out of 8 radial channels. After injecting solution into the microchannel, 10 V was applied between center pipette tip and the end of channel for preconcentration step. With the voltage bias, the ion depletion zone was formed at the anodic side of the Nafion and microparticles were started to be preconcentrated as shown in Figure 4.2 (a). Since the strong vortical flow inside the depletion zone induces a weak vortex outside the depletion zone[18, 46, 47], the shape of the preconcentrated particles involved both compact plug and vortical cloud at the boundary of depletion zone. As dc bias was applied continuously at the device, the preconcentrated plug and vortical cloud of microparticles were propagated to the

center, while solvent in the center pipette tip was flushed out toward the rim at each branches. After 2 hours of operation, most of microparticles contained in the pipette tip were gathered at the bottom of the pipette tip as shown in Figure 4.2 (b). In this experiment, 35 μL of the microparticle solution was operated for 2 hours to become 3 μL of concentrated solution. The theoretical concentration ratio was calculated by dividing the final volume by the initial volume, which results in about 11.7 fold of preconcentration factor. To calculate the experimental result of concentration ratio after preconcentration, the number density of microparticles at the bottom of the center pipette tip between before and after preconcentration step was compared. Region of interest (ROI) to count the number density was set to be an annular shape as shown in Figure 4.2 (b). We excluded the center region where the pipette tip was inserted. Before preconcentration step, ~80 particles were counted inside the ROI, while ~800 particles were counted inside the ROI after preconcentration step (particles within the same focal length was only counted). Thus measured preconcentration factor after the operation was calculated to be 10 fold. Dividing the experimental concentration ratio by the theoretical concentration ratio, it showed 85.5 % of particle recovery ratio as in Figure 4.2 (c). This result proved that most of particles were captured by the depletion zone and collected to the center pipette tip. While previously reported preconcentrating techniques can preconcentrate the analytes only in a small volume (few pL-nL) of microchannel, the radial preconcentrator in this work has advantages over them since it can collect all the analytes into relatively large volume of pipette tip (few μL). Although we

demonstrated with the 10 μL pipette tip (white tip), we can achieve higher preconcentration ratio if one uses a larger volume of pipette tip (blue tip of 1 mL). However, in this case, the preconcentration time should be longer, so that it is necessary to leverage the preconcentration ratio and the operation time according to one's discretion.
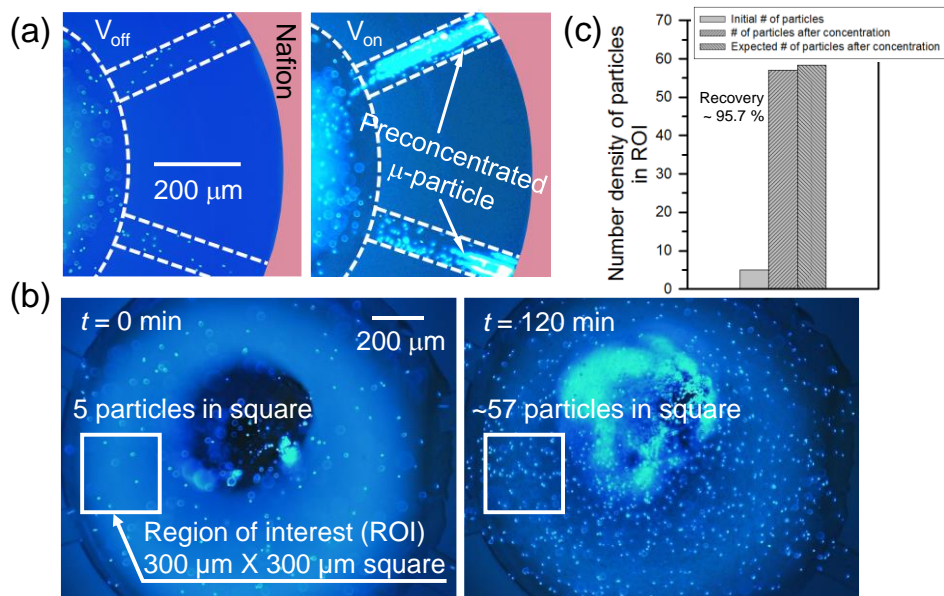
Figure 4.2 (a) Microscopic snapshots of microparticle preconcentration, demonstration using Nafion-junction device. When dc bias was applied, particles showed both compact plug with vortical cloud. (b) Microscopic image at the bottom of center pipette tip at $t = 0$ min (before preconcentration, left image) and $t = 120$ min (after preconcentration, right image). Number density of particles at the same focal length in the ROI was compared. (c) Diagram of number density of particles from (b) and number density of particles calculated by the volume ratio before and after preconcentration step.

4.3.1.2. Fluorescent dye demonstration

Since we confirmed that most of particles in the pipette tip were preconcentrated at the bottom of the pipette tip while solvent flushed out, small analytes (200 nM concentration of Alexa 488 fluorescent dye) with 1mM potassium chloride buffer background solution was used to demonstrate both preconcentration and extraction steps. Figure 4.3 (a) showed the preconcentration of fluorescent dye at a 16-way radial device with a voltage of 10 V. At 10 seconds, fluorescent dyes started to form plugs at each anodic side of Nafion and the preconcentration plugs propagated to the center pipette tip as shown in the right image of Figure 4.3 (a). In order to quantify the preconcentration efficiency, electroosmotic velocity ($v_{eof} = \varepsilon_0\varepsilon_r\zeta|\mathbf{E}|/\mu$ where ε_0 and ε_r the permittivity of free space and relative permittivity of sample solution, respectively and μ the viscosity of sample solution and ζ the zeta-potential of microchannel wall and $|\mathbf{E}|$ the applied electric field to each microchannel) was calculated for measuring the operation time. Here the parameters were given as $\varepsilon_0 = 8.854 \times 10^{-12}$ CV^{-1}m^{-1}, $\varepsilon_r = 80$, $\mu = 0.001$ Nsm^{-2}, and $\zeta = \sim -80$ mV[139, 140]. Since the radial preconcentrator had a parallel connection structure and the length of each channel was fixed at 7 mm, the average electric field across at each branch channel was assumed to be constant at 14 V/m with 10 V constant bias. Then v_{eof} was calculated to ~80 μm/s on each microchannel. Multiplying the width and height of each microchannel (100 μm and 50 μm, respectively), volume flow rate induced by electroosmotic flow (vol_{eof}) was calculated to be ~20 nL/min on each microchannel. Three types of device with 4, 8, and 16 branch channels were prepared to verify

device operation time according to electroosmotic flow and number of channels, and we calculated the time taken for the solution to decrease from 35 µL to 1 µL using the above volume flow rate, giving the operation time as $T_{op} = (V_{initial} - V_{final})/nvol_{eof}$ (where T_{op} the device operation time, $V_{initial}$ and V_{final} the initial and final volume, respectively and n the number of branch channels). The calculated T_{op}s were ~360 minutes, ~180 minutes, and ~90 minutes for $n = 4$, 8, and 16 branch channels, respectively. Experimental T_{op}s were measured (time taken the initial volume of 35 µL reduced to 1 µL) were ~190 minutes, ~120 minutes, and ~75 minutes on average for 4, 8, and 16 branch channels, respectively as shown in Figure 4.3 (b). Main reason for the difference between the calculated device operation time and measured device operation time was pressure driven flow. Corresponding flow rates of pressure driven flow are ~20 nL/min, ~10 nL/min and ~5 nL/min for 4, 8 and 16 branch channels. Since pressure difference was induced by the level difference between center pipette tip and each reservoir at the end of each branch, more branch caused less pressure difference. Thus, the flow rate from pressure driven flow should inversely proportional to the number of branches as we shown above.

Since 30 µL and 50 µL solution was preconcentrated until $V_{final} = 5$ µL, we aimed to achieve the preconcentration ratio was 6 and 10 fold, respectively. Previous ICP works, such as million-fold preconcentrator[98], the analytes were preconcentrated inside a microchannel and the factor was measured again inside the microchannel, whereas our radial preconcentrator measured the concentration ratio after extracting the preconcentrated analyte out of the microchannel so that there should be an

inevitable dilution occurred in micro-to-world interfacing. With setting the maximum factor as 10^6, one may expect the maximum factor inside microchannel of 100 ($10^6 \times 100$ μm (plug length) $\times$ 100 μm (plug width) $\times$ 50 μm (plug height) / 5 μL). However, since our design is 'bufferchannel-less' and there should be inevitable dilution at world-to-chip interfacing, the factor obtained by volume ratio (initial volume / final volume) would provide more accurate estimation than the factor by above simple calculation. While ~10 fold can be considered low, it is expected that one can accomplish a preconcentration ratio higher than 10-folds using a larger pipette tip at the center reservoir.

In order to extract the preconcentrated sample, the solvent at the entire rims was firstly removed and remaining preconcentrated solution at the center was extracted by just pulling out the pipette. The extracted solution was injected into straight microchannel of 15 μm height and 100 μm width, and the intensity of the fluorescent dye was analyzed using image J. Recovery ratio of the dye was calculated as $R = V_{ext}M_{ext}/V_{initial}M_{initial}$ where V_{ext} the extracted solution volume, $M_{initial}$ and M_{ext} the initial and extracted molar concentration of the dye, respectively. The value of R by the experimental data gave ~79 %, and ~4.5 fold of preconcentration factor for 30 μL solution and ~75 %, and ~7.5 fold of preconcentration factor for 50 μL as shown in Figure 4.3 (c). We expected the preconcentration ratio (the ratio of the initial sample volume to the recovered sample volume) of 6 fold when we injected 30 uL of initial sample and recovered 5 uL of preconcentrated sample. In the case of 50 uL initial volume, recovered volume was 5 uL so that the expected value was 10 fold.

However, experimentally measured preconcentration ratio was 4.5 fold and 7.5 fold. This small discrepancy against the expected preconcentration ratio was due to the natural diffusion before dc bias was applied and sample loss due to induced advection when the pipette tip was pulled out from the device.
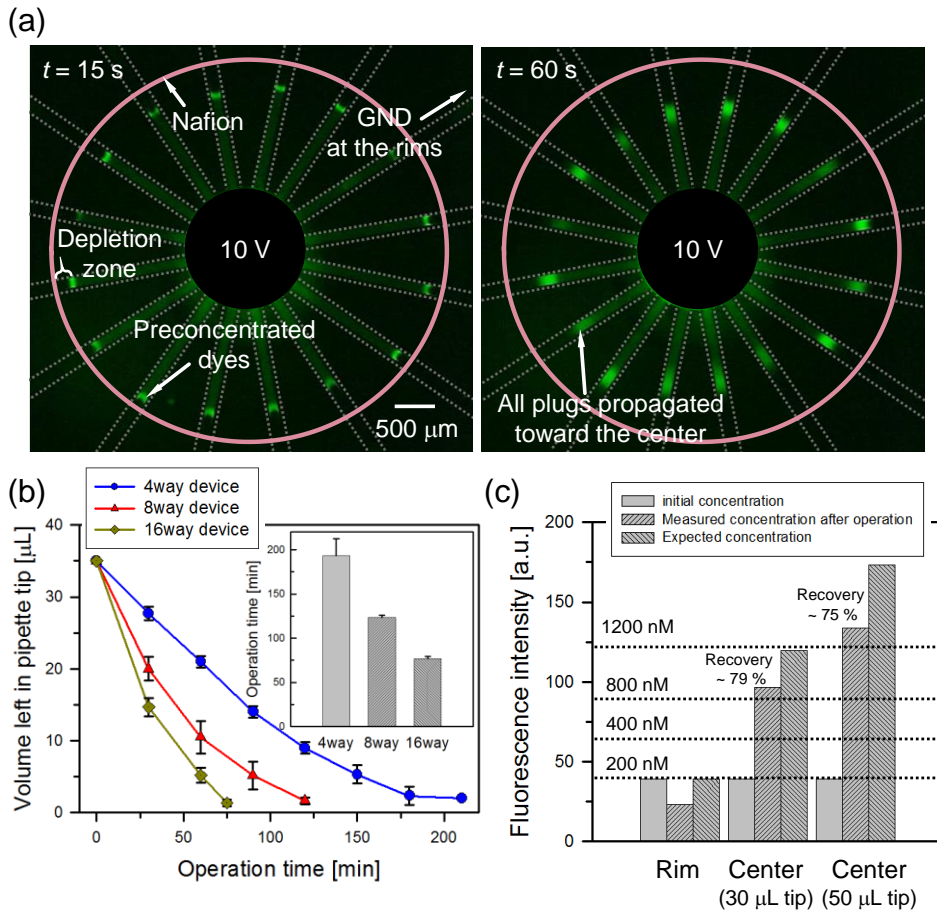
Figure 4.3 (a) Microscopic snapshots of fluorescent dye preconcentration demonstration using 16-way Nafion-junction device. Preconcentrated dye plugs formed (left image) and propagated toward the center (right image) with applied dc bias. (b) Graph showed the amount of solution left in the pipette tip as the device operated and the calculated T_{op} for 4-, 8-, and 16-way device. (c) Diagram showed the concentration of $M_{initial}$ and M_{ext} compared to expected concentration by the volume ratio before and after preconcentration step.

4.3.1.3. dsDNA demonstration

The preconcentration and extraction of dsDNA was also conducted to verify the possibility of the radial preconcentrator/extractor to BioMEMS applications. The initial concentration of dsDNA was ~16.6 ng/μL with 0.1 X PBS and 10 V bias was continuously applied at 8-way radial device. As shown in Figure 4.4 (a), preconcentrated plugs of dsDNA was successfully converged to the center pipette tip, while solvent was flushed out toward the rims. After preconcentration step, preconcentrated samples were extracted in the same manner as the fluorescent dye experiment, expecting 10 fold of preconcentration ratio (30 μL sample solution was preconcentrated to 3 μL). The extracted solution was analyzed with the spectrophotometer and the results are shown in Figure 4.4 (b). The concentration of DNA extracted from the center pipette tip measured to be 87.8 ng/μL on average with a standard deviation of 31.2 showing a concentration ratio of ~4.9 fold compared to the initial concentration. Considering $V_{initial}$ and V_{ext}, the expected concentration ratio was 10 fold. The measured preconcentration ratio of dsDNA showed large deviations due to the same reason stated in previous section. Furthermore, dsDNA has lower zeta potential[141] than that of fluorescent dye[142] used in this work, leading to high probability of leaking through the ion depletion zone (*i.e.* lower preconcentration factor). The recovery ratio, R by the experimental data gave ~51.3 % of dsDNA.

With a view of recovering preconcentrated sample for chip-to-world analysis, this bufferchannel-less radial preconcentrator has advantages over previous reported

radial preconcentrator[135]. It demonstrated two types of radial preconcentrator; (i) empty chamber type and (ii) finned chamber type. The empty chamber type has the chamber volume of 100 nL ($\pi \times 1.2$ mm$^2 \times 20$ μm) and the preconcentrated sample volume of 20 nL (700 μm $\times$ 700 μm $\times$ 40 μm) and the preconcentration factor was measured at 168 fold. Thus, there should be 1/250 fold dilution for chip-to-world analysis, if 20 nL of 168 folded sample was extracted by laboratory apparatus such as pipette. (We assumed that 5 uL is the minimum volume for delivering the sample to another conventional analyzer). Also, the finned chamber type has the chamber volume of 1.5 uL ($\pi \times 3.5$ mm$^2 \times 40$ μm) and the preconcentrated sample volume of 10 nL (400 μm $\times$ 700 μm $\times$ 40 μm) and the preconcentration factor was measured to be 20 fold. Thus, there should be 1/500 fold dilution for chip-to-world analysis, if 10 nL of 20 folded sample was extracted by laboratory apparatus. Furthermore, both structures can preconcentrate the sample which was already filled inside the chamber so that the extracted sample volume is always limited by the chamber volume. Therefore, this comparison led that this radial preconcentrator is suitable for chip-to-chip analysis, not for chip-to-world analysis. Note that there should be additional structure to prevent an avoidable dispersion even in chip-to-chip analysis.
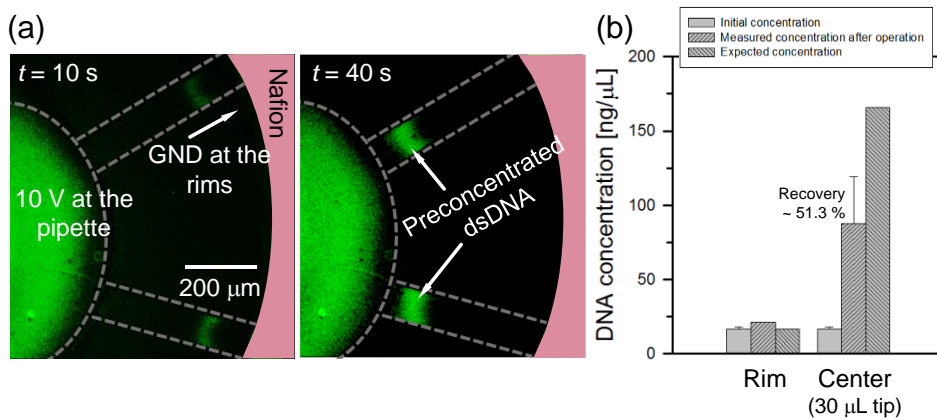
Figure 4.4 (a) Microscopic snapshots of dsDNA preconcentration demonstration using Nafion-junction device. (b) Diagram showed the concentration of $M_{initial}$ and M_{ext} compared to expected concentration by the volume ratio before and after preconcentration step.

4.3.2. Printed-electrode device

With the Nafion-junction device, the negatively charged molecules (microparticle, fluorescent dye, and dsDNA) were able to be preconcentrated and extracted because the convective drag force and electrophoretic force affected to the negatively charged molecules in the opposite direction. However, since those forces aligned in the same direction in the case of positively charged species such as rare earth elements, heavy metal and positively charged amino acid (lysine, arginine, histidine, *etc*), it was difficult to preconcentrate positively charged molecules on the cation-selective membrane device. To preconcentrate the positively charged molecules in the ICP preconcentration device, anion-selective membrane was needed to be used as a nanoporous membrane. However, utilization of either cation- or anion-selective membrane hindered the versatility of the device. Consequently, it is highly required to have a tunable preconcentrating device for either positively- or negatively-charged analyte at one's discretion. In this work, we fabricated the silver electrode patterned radial preconcentrator for switchable Faradaic reaction on the printed electrode for preconcentrating either types of charged molecules[137, 143].

4.3.2.1. Schematics of printed-electrode device

The schematics of the preconcentration by Faradaic reactions at the single straight microchannel were shown in Figure 4.5 (a) and 4.5 (b) for negatively- (50 nM of SRB) and positively-charged analyte (50 μM of rhodamine 6G), respectively. Due to the nonspecific binding of cationic dye to negatively changed PDMS surface, one

need to use thicker cationic dye than anionic dye (but they have similar fluorescent intensity). The direction and thickness of blue arrows in Figure 4.5 (a) corresponded to the directions of electroosmotic flow (EOF) (along with the applied electric field) and the magnitudes of EOF (greater inside the ion depletion zone than outside the zone due to the amplified electrokinetic response only inside the zone[46]), respectively. In case of negatively charged molecules, the directions of EOF and electrophoresis (EPH) ($\mathbf{F}_{EPH}$ in Figure 4.5 (a)) are opposite to each other and are preconcentrated on the same principle as conventional ICP preconcentration. In case of positively charged molecules, the directions of EOF and EPH are same. However, since the forces received by the molecules inside the depletion zone is stronger than the forces received outside the depletion zone, preconcentration occurs with similar principle as isotachophoresis[90]. Without pressure driven flow (red arrow in Figure 4.5 (a) and 4.5 (b)), the sample flows toward center pipette so that the sample in the pipette is going to be diluted. To prevent this backward flow, we intentionally applied pressure driven flow in this printed-electrode device. While the sample was filled from the pipette tip to the reservoir at the ends of radial channels in the Nafion-junction device, the sample was filled from the pipette tip, but the filling was stopped in the middle of microchannels in this printed-electrode device. Thus, printed-electrode device always has a pressure driven flow toward the rim.

Since major carriers at this reaction were hydrogen ion and chloride ion, we used Tris-HCl buffer as the buffer solution to contain sufficient hydrogen and chloride ions, while keeping the buffer solution as weak acid (pH = 5.6). When voltage was

applied to the bulk pipette tip and the printed electrode, reduction and oxidations occurred at the cathode and anode, respectively by the electrochemical reaction. Due to the extremely large resistance of the ion depletion zone, the ionic current through the electrode was less than 10 nA so that the generations of gaseous byproducts were largely suppressed especially after forming the ion depletion zone. Under this situation, the gaseous byproducts from the electrochemical reactions that generated near the bulk pipette tip were dissolved into the bulk solution so that the ion concentration near the bulk pipette tip was maintained. Any bubbles at patterned electrodes were observed in the experimental condition in this work. Thus, the ion depletion zone near the printed electrode can be utilized as preconcentration barrier.
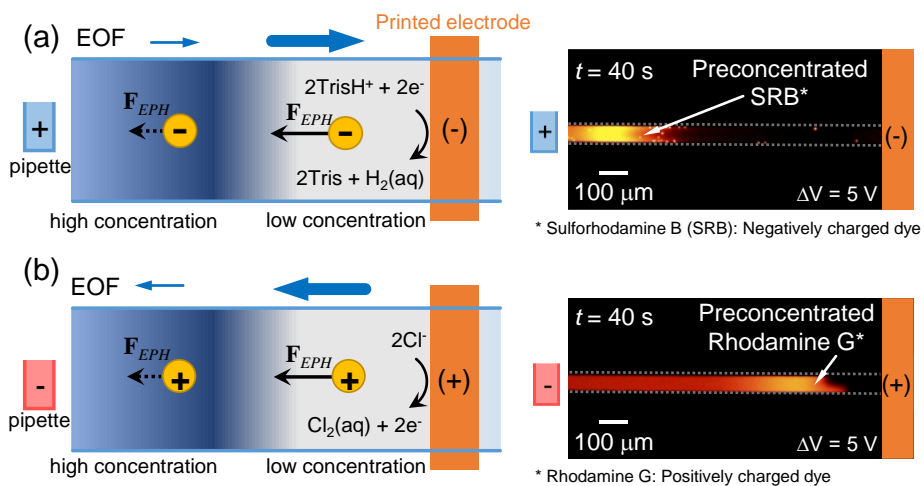
Figure 4.5 (a) Schematic diagram for the generation of depletion zone by Faradaic reaction (anode: pipette, cathode: printed electrode) to preconcentrate negatively charged molecules. Microscopic snapshot of SRB demonstration was shown in the right image. (b) Schematic diagram for the generation of depletion zone by Faradaic reaction (anode: printed-electrode, cathode: pipette) to preconcentrate positively charged molecules. Microscopic snapshot of Rhodamine 6G demonstration was shown in the right image.

4.3.2.2. Gaseous production at the printed-electrode device by Faradaic reaction

When a voltage (V) is applied between pipette tip and the printed electrode as shown in Figure 4.6 (a), anions are generated by the reduction occurred at the cathode and cations are generated by the oxidation occurred at the anode. Cathode and anode can be switched for each case, but the reactions are identical. The electrode reactions are given as followings.

[Cathode]

$4H^+ + 4e^- \rightarrow 2H_2$ (g)$E^0 = 0.00$ V

$6H_2O + 6e^- \rightarrow 6OH^- + 3H_2$ (g)$E^0 = -0.83$ V

$OH^- + TrisH^+ \rightarrow Tris + H_2O$

[Anode]

$OH^- - 4e^- \rightarrow O_2$ (g) $+ 2H_2O$ $\quad E^0 = 0.40$ V

$2H_2O - 4e^- \rightarrow 4H^+ + O_2$ (g)$E^0 = 1.23$ V

$2Cl^- - 2e^- \rightarrow Cl_2$ (g)$E^0 = -1.36$ V

[Overall]

$4H_2O \rightarrow 4H_2$ (g) $+ 2O_2$ (g)

$2Cl^- + 2TrisH^+ \rightarrow 2Tris + Cl_2$ (g) $+ H_2$ (g)
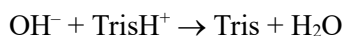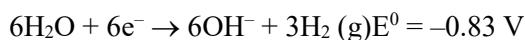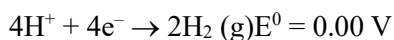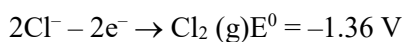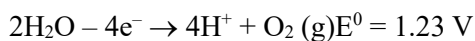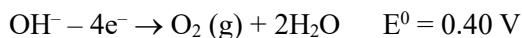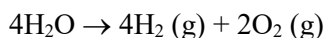
In the given configuration as shown in Figure 4.6 (a), the relation between the current density and the gas concentration are governed by diffusion equation (an electromigration can be negligible since the target species in this analysis is uncharged gas),

$$\frac{\partial c_{gas}}{\partial t} = -\frac{\partial J}{\partial x} = D_{gas} \frac{\partial^2 c_{gas}}{\partial x^2} \tag{4}$$

where the c_{gas} is the concentration of produced gases, J is the current density, and D_{gas} is the diffusivity of the gases in the water. Under the steady state assumption, left side of the equation (4) becomes zero and then the concentration of the produced gases becomes linear as

$$c_{gas} = Ax + B \tag{5}$$

The constant A and B were obtained with the boundary conditions of

$$c_{gas} = 0 \text{ at } x = 0 \text{ and } J = -D_{gas}\frac{\partial c_{gas}}{\partial x} = \frac{I}{SF} \text{ at } x = L \tag{6}$$

where I is the current measured by the experiment, S is the cross-sectional area of the microchannel, and the F is the Faradaic constant. Considering the measured current at the Supplementary Figure 4.6 (b) and 4.6 (c) and the production ratio from the Faradaic reactions above, we can calculate the concentration of each gases produced during the experiment. From the boundary conditions, the constant $A = I/P_R D_{gas}FS$ and $B = 0$, where P_R is the production ratio from the Faradaic reactions of each gases. Substituting approximate value for each parameter, the order of produced concentration of each gases during experiment are obtained as followings.

$$c_{H_2}\Big|_{electrode} = \frac{IL}{2D_{H_2}SF} \sim \frac{10^{-9}\cdot 10^{-3}}{2\cdot 10^{-8}\cdot 10^{5}\cdot 10^{-4}\cdot 10^{-5}} \sim O(0.1), \tag{7}$$

$$c_{O_2}\Big|_{electrode} = \frac{IL}{4D_{O_2}SF} \sim \frac{10^{-9}\cdot 10^{-3}}{4\cdot 10^{-8}\cdot 10^{5}\cdot 10^{-4}\cdot 10^{-5}} \sim O(0.1) \text{ and} \tag{8}$$

$$c_{Cl_2}\Big|_{electrode} = \frac{IL}{5D_{Cl_2}SF} \sim \frac{10^{-9} \cdot 10^{-3}}{5 \cdot 10^{-8} \cdot 10^5 \cdot 10^{-4} \cdot 10^{-5}} \sim O(0.1). \tag{9}$$

Since the solubility of H, O, and Cl gas at 1 atm and 25 °C are 0.8 mM, 100 mM, and 1 mM, respectively[144], we can conclude that the gases produced during the experiment are dissolved in the bulk solution.
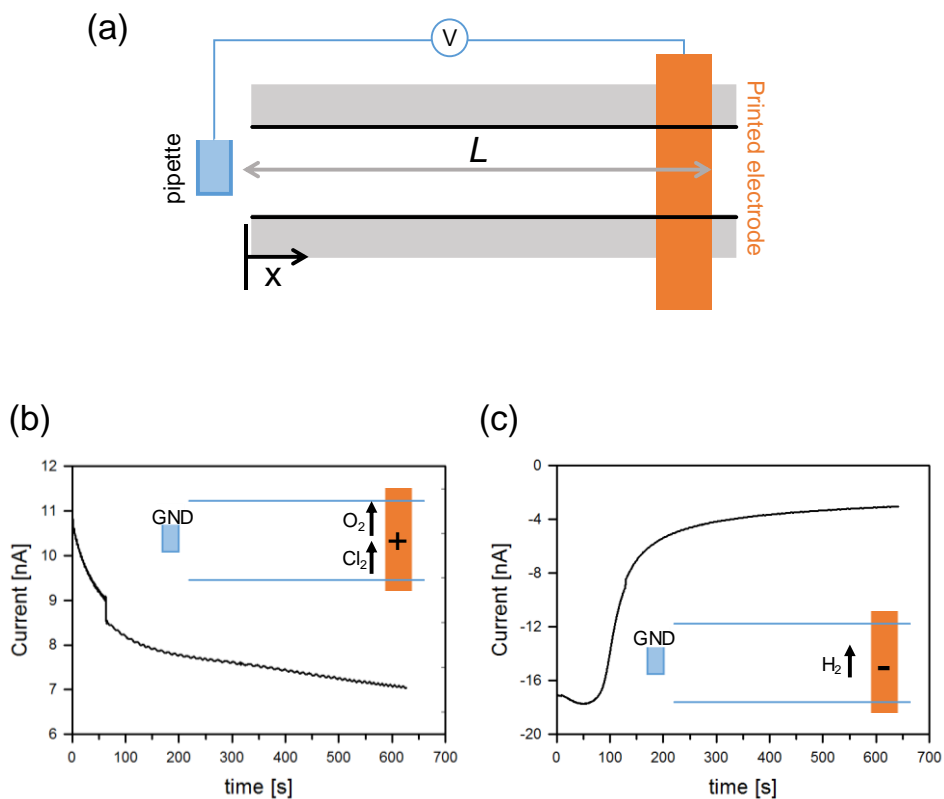
Figure 4.6 (a) Succinct schematics of the printed-electrode device and the I-t curve between pipette and printed electrode. (b) when printed-electrode is anode (5 V is applied at the printed-electrode). and (c) when printed-electrode is cathode (-5 V is applied at the printed-electrode).

4.3.2.3. Experimental demonstration of printed-electrode device

When the printed electrode was a cathode, a preconcentrated plug of negatively charged fluorescent dye was formed in the direction to the pipette tip by the electric field gradient caused by the ion depletion zone near the printed electrode (Figure 4.5 (a)), and *vice versa* (Figure 4.5 (b)) for positively charged dye. Since the surface charge on the wall of microchannel was negative, positively charged dye received electrical attraction from the channel wall and the progress of the preconcentration plug was slower than that of the negatively charged dye.

These principles were directly applied to the 64-way radially arranged microchannel. The channels were attached on the printed electrode and the results were shown in Figure 4.7 (a) and 4.7 (b). The voltage applied at the center pipette tip was fixed as ground for both experiments. To preconcentrate the negatively charged molecules, printed electrode was used as a cathode and *vice versa*. The preconcentration plugs of negatively charged dye were formed and started to propagate to the center within only 3 seconds under 15 V bias (Figure 4.5 (c); preconcentration factor of 2 within 3 seconds) while 10 seconds were needed for the positively charged dye to form plugs and start to propagate to the center (Figure 4.5 (d); preconcentration factor of 2 within 10 seconds) under the same dc bias as we expected. Due to gas bubble generation at the patterned electrode and pH variation for a long-term operation exceed an hour, the printed-electrode preconcentrator is better suit for the platform of on/off sample detection using the preconcentrated sample at the center reservoir. However, it is still useful as the preconcentrator and

online collector when the target volume is small so that total operation time is less than an hour. Also patterning the chemically stable metal electrode such as gold or non-polarizable electrode would be alternative strategy for longer operations.
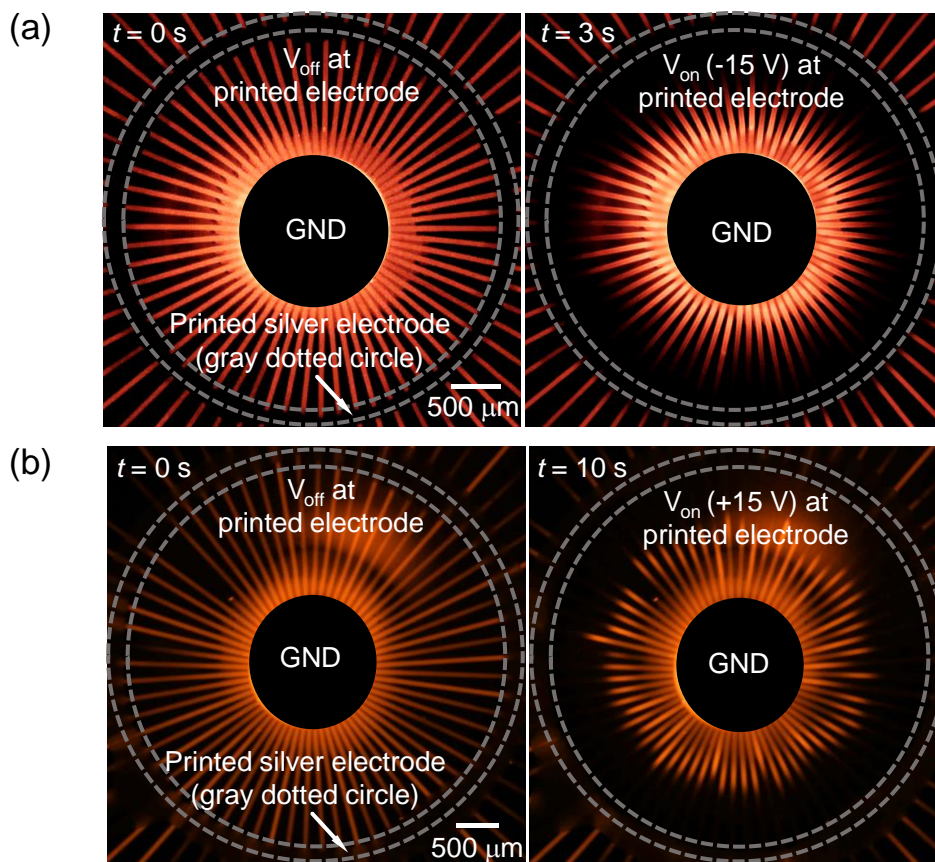
Figure 4.7 Microscopic snapshots of preconcentration demonstration of (a) SRB and (b) Rhodamine 6G using 64-way printed-electrode device.

4.4. Conclusions

In this work, we proposed a bufferchannel-less micro/nano fluidic device with a simple extraction method while the useful preconcentration factor was maintained for downstream analysis. With the bufferchannel-less design, we minimized the unnecessary electrical connection and employed a radial type microchannel network to maximize the microchannel/nano membrane interface which results in significantly improved throughput and stability. Most importantly, the preconcentrated samples were easily recovered by just pulling out the center pipette tip. With the Nafion-junction device, ICP was used as the main mechanism and preconcentration of 1 μm-size polystyrene particle was firstly demonstrated to verify the basic operation of the device with the ~85.5 % of recovery ratio. The preconcentration and extraction of fluorescent dye and dsDNA was demonstrated and we could recover ~79.0 % and ~51.3 % of analytes in the whole pipette tip within analyzable volume, respectively. Operation time of device was also compared depending on the number of branch channels. With the printed-electrode device, a Faradaic reaction was used as the main preconcentration mechanism. To verify the device operation, preconcentration of either types of charged molecules were demonstrated at the single straight microchannel. Then, these principles were directly applied to the 64-way radially arranged device and preconcentration was successfully demonstrated.

Despite of these advantages, current design was not suitable at high buffer

concentration. We performed additional experiments at 10 mM and 100 mM. The results showed that a constant preconcentration plugs were successfully generated at 10 mM, but serious bubble generation due to electrolysis was observed at 100 mM. The original bufferchannel-less preconcentrator had demonstrated at 1X PBS condition, but it had only one microchannel[119]. The measured current level in bufferchannel-less device is about 4 times higher than one in buffered device because the ionic current can flow simultaneously through electrolyte above the membrane and through the membrane. It is more serious in the radial concentrator because the current is linearly proportional to the number of radial branches and the buffer concentration. For example, 10 nA was measured in typical buffered device at 1 mM and 10 V[107] so that ~192 uA should flow in 16 channel bufferchannel-less radial concentrator at 100 mM and 30 V, *i.e.* 10 nA × 4 (due to bufferchannel-less) × 16 channels × 100 (due to 100 mM) × 3 (due to 30 V). At such huge current, bubble generation on patterned electrode should be non-negligible compared to the micro-bubble generation at lower current. The ring electrode can be located within an outlet reservoir allowing the evacuation of generated bubbles. However, as shown in Supplementary Figure 2, the bubble was generated also in the center reservoir as well to disconnect electric field.

This is the clear limitation of this bufferchannel-less radial preconcentrator. Thus, further modifications should require for proper operation at the high concentration such as changing electrode material to suppress electrolysis (for example, a material having higher surface to volume ratio such as carbon felt) or thicker Nafion

patterning to minimize leakage current above the membrane and structural modification for removing gas bubble (for example, hydrophobic coating inside the pipette tip and electrode surface leads easy evacuation of the bubble). However, there are several applications that should work at this low buffer concentration less than 10 mM. For example, environmental monitoring or food monitoring applications usually dealt with tap water from faucet or fresh water from river (or food), etc. whose total ionic concentration is less than 10 mM (10 mM is the upper limit of potable water). A few biological applications also required a dilution at low concentration condition. While drying could be used, it is to concentrate not only the particles but also the electrolyte ions. On the other hand, ICP method concentrates only the particles while maintaining the electrolyte ion concentration. Thus, one can choose the suitable preconcentration method depending on the requirements. For example, drying method is better if the concentration of background ion does not matter. However, since there are many cases where background electrolyte should not be concentrated[145, 146], the ICP preconcentrator is also useful in those cases. Thus, while our radial layout has the clear limitation as mentioned, it is still feasible on those applications. In this sense, the bufferchannel-less radial preconcentrator and online extractor was expected for handy platform of sample preparation step in various biomedical and environmental applications requiring an appropriate preconcentration ratio.

Chapter 5. Concluding Remarks

A micro/nanofluidic platform for direct target blood cancer gene detection was fabricated and tested using ion concentration polarization and specific binding of dCas9 protein. This methodology has novelty on real-time target specific DNA detection without PCR amplification. Altered electrophoretic mobility by dCas9-DNA binding enabled the target gene detection, and as a step for clinical approach, the target DNA fragment ratio was reduced to 1 %. Next, for clinical sample refinement and other BioMEMS applications, A highly efficient radial preconcentrator-extractor device was devised. In the process of fabrication, a new Nafion patterning method was tried and an experiment was conducted to replace the selective membrane with and electrode. Both two researches have a significant potential to contribute to an appropriate technology, and when they are combined, it is expected to realize a rapid and simple on-off hematological cancer diagnosis chip for clinical samples.

Appendix

Appendix A. Inkjet-printed nanoporous junction

A.1. Introduction

There are a wide variety of methods such as photolithography, imprint lithography, and laser lithography, which are the most commonly used methods for fabricating nanostructures. In the photolithography method, the desired pattern shape is transferred with a mask after applying SU8 on the entire substrate. After that, when irradiated with ultraviolet light, only the pattern is cured, and when developed, only the cured portion remains. This method is resulting in a large material dissipation since the entire area of the substrate except for the pattern is discarded. In particular, since nanoporous materials such as Nafion are expensive, this method is not suitable. In addition, there is a problem that the properties of the substrate are limited due to ultraviolet irradiation.

Most of the inkjet printing method uses a piezoelectric method, and since only a portion corresponding to a desired pattern is ejected from the nozzle, material waste can be minimized. Existing printers for MEMS process have advantages in that ink can be easily replaced and various substrates can be selected by adjusting process conditions[147]. However, accuracy is lowered compared to the existing process method and the cost is expensive.

Therefore, in this study, low-cost inkjet conventional printer is utilized by adjusting the viscosity of the solution to be printed similar to that of printer ink and

then pattering was conducted regardless of its shape.

A.2. Device and materials

Printer preparation

In this study, a piezoelectric printer (K-100, EPSON, JAPAN) was used for Nafion printing. When printing on a glass substrate instead of paper, the paper injection recognition sensor was directly manipulated to send an electrical signal to the printer to consider as the paper passing by as shown in Appendix Figure A. 1. A micro glass (24 mm x 60 mm, MARIENFELD, USA) was placed on the position where the ink was to be sprayed. Since a 1 mm-thick slide glass can destroy the nozzle, a 0.13 ~ 0.16 mm-thick microglass was used in this experiment.

O₂ Plasma treatment

Super hydrophilic substrate

● Oxide ion ● Other ions (C, H, etc)

Nafion ink

EPSON K-100
inkjet printer(piezoelectric)
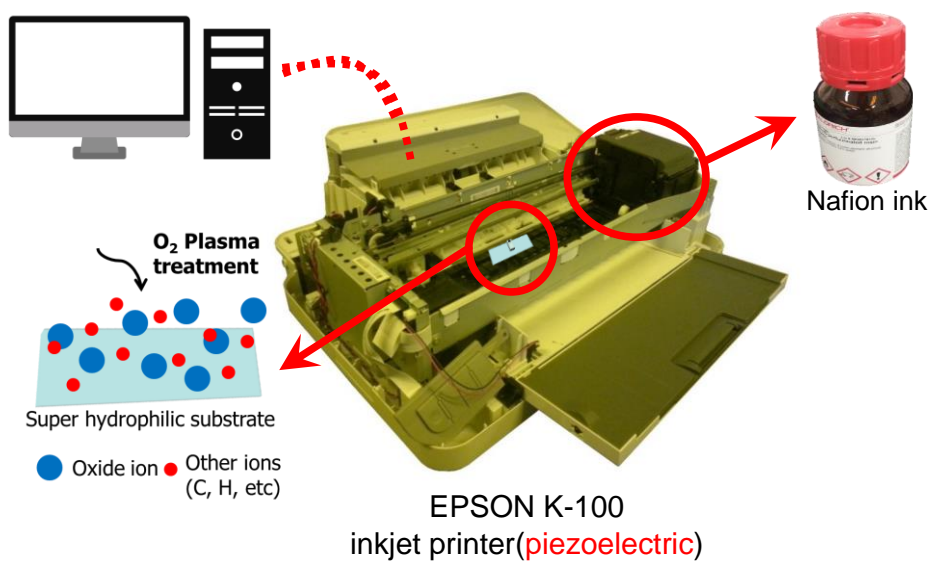
Appendix Figure A.1 Concept diagram of Nafion ink printing using EPSON K-100 printer. Replace ink to Nafion ink in the ink cartridge, and place the glass substrate to be printed at the position where the nozzle is sprayed. In advance, the glass substrate was plasma-treated to make the ink spread easily. Finally, printing was carried out through a computer connected to a printer.

Nafion ink preparation

In this study, a Nafion resin solution (Nafion wt 20%, Sigma-Aldrich, USA) was used as a material for making the nanoporous membrane. The Nafion resin solution acts as a nanoporous membrane when the alcohol-water-based solvent evaporates. Ink viscosity was the most important factor in piezoelectric printing because it affects the surface tension of ink[148]. Therefore, in order to match the viscosity of the EPSON printer ink (T1371, EPSON, JAPAN) and Nafion-distilled water mixed solution (Nafion ink), the viscosity was measured and adjusted using a vibratory viscometer (SV-10A, A&D). Appendix Table A. 1 shows the results of measuring the viscosity of each material.

Material	Viscosity	Mixture ratio to DI water
DI	1	
Commercial ink	3.89	
Nafion solution	6.15	1:4
Nafion solution	5.32	1:5
Nafion solution	3.26	1:7
Nafion solution	2.49	1:9

Appendix Table A.1 Viscosity measurement results for several substances. The viscosity of Nafion solution diluted one over eighth was most similar with the that of commercial ink. So the dilution rate was determined to be one over eighth.

A.3. verification of printed Nafion through ion concentration polarization

Nafion printing results using EPSON inkjet printer were shown in Appendix Figure A. 2 (a). The desired shape (line, circle, word) could be printed simply by writing the desired character or shape in the word process program on the computer which connected to the printer. In addition, the printed circular shaped Nafion was subjected to plasma treatment and combined with a channel of radial structure as shown in right side of Figure A. 2. (a). Appendix Figure 2. (b) shows the results of the concentration experiment of the device with the Nafion loaded by the conventional surface patterning method and the device with the Nafion loaded by the Nafion printing method. As in the experimental results, Ion transport and perm-selectivity of the printed Nafion occurred well by confirming that the preconcentration of the florescence dye using the ICP showed similar results compared to the surface pattering method. Furthermore, to identify the electrical characteristics of the Nafion surface patterning method and Nafion printing method, voltage-current was measured in the ICP condition by increasing the voltage from 0 V to 10 V with incremental rate as 0.2 V/15 second for the device with the Nafion patterned by surface pattering, surface patterning with dilute Nafion, and printed Nafion. The results showed that there was no significant difference in the ion transport power for these three methods since the electrical conductivity values were similar for all three methods in the overlimiting region.
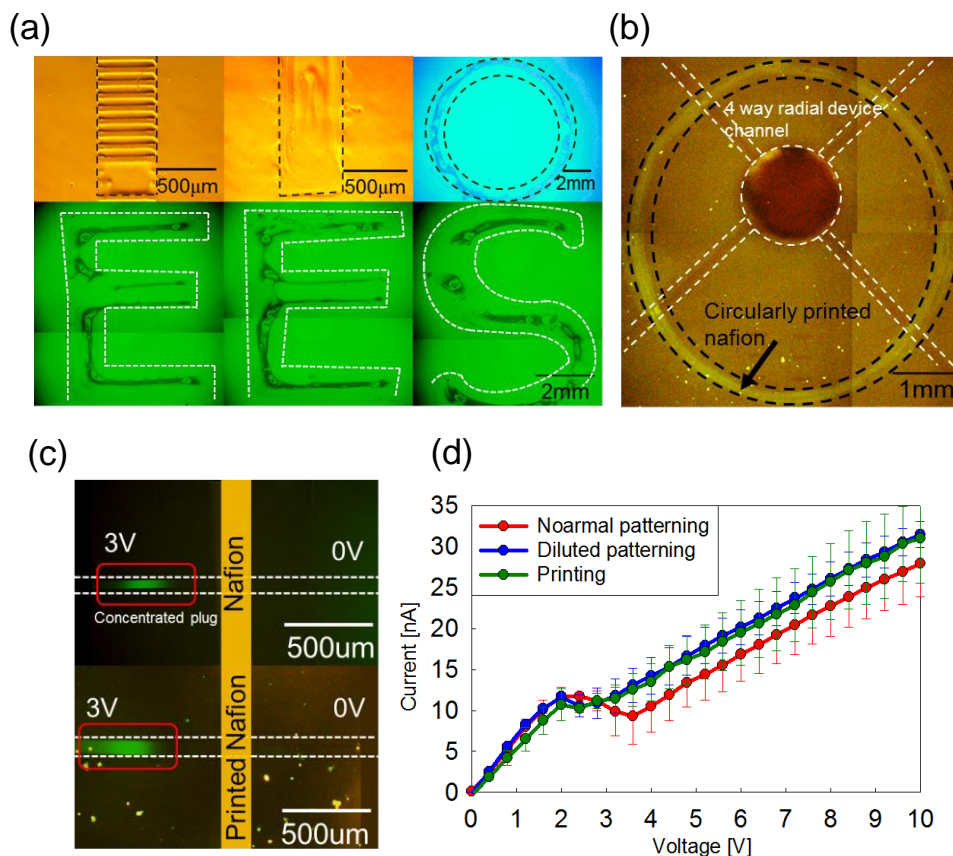
Appendix Figure A.2 (a) Results of printing various shapes using Nafion ink. (b) Microchannel bonded to circularly printed Nafion. (c) Comparative experiment for preconcentration of fluorescence dye between printed Nafion and surface patterned Nafion. (d) I-V characteristics graph of surface patterned Nafion (w/, w/o dilution), and printed Nafion.

Appendix B. Radial preconcentrator and extractor integrated with PCB board

B.1. Fabrication of device integrated with PCB board

For the symmetrical and stable voltage supply on radially shaped device, gold electrode was manufactured on the PCB board according to the voltage applying shape of the radial preconcentrator as shown in Appendix Figure B. 1 (a). It was expected that the preconcentrated sample would be easily extracted and the that the loss would be reduced while extracting since PCB board enables the system to free from electrode injection.

However, since the PCB board and PDMS had poor adhesive property to each other, a thin PDMS spin coating was applied to the PCB board and Nafion was loaded on it in a circular shape, and then the spin-coated PDMS and radial device were adhered by plasma bonding method as shown in Appendix Figure B. 1 (b).
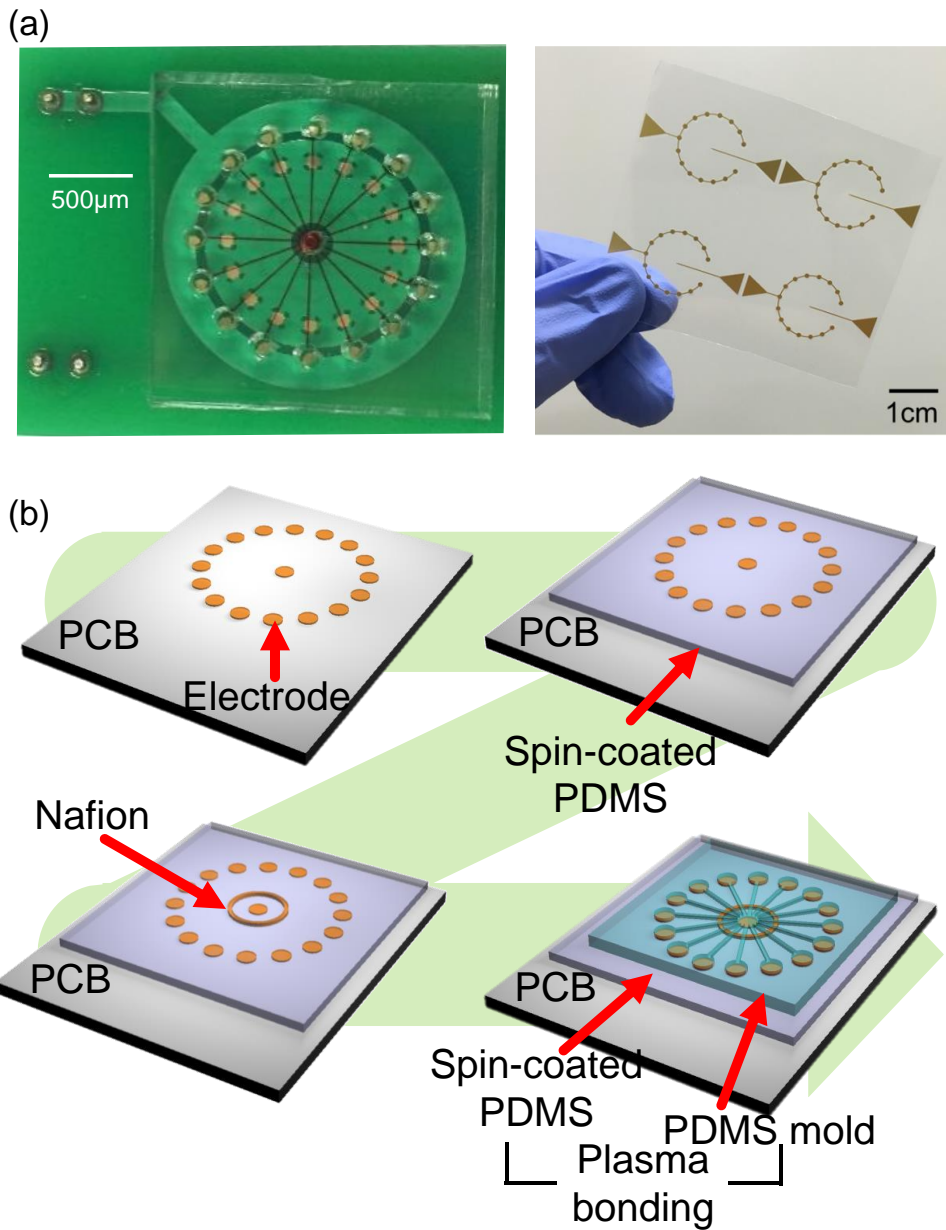
Appendix Figure B.1 (a) PCB board for radial preconcentrator. (b) fabrication process of PCB-PDMS device.

## B.2. Experimental demonstration of PCB-substrate device

As shown in Appendix Figure B. 2 (a), Fluorescence dye (2 nM, Alexa 488) was preconcentrated and extracted through a device which was manufactured based on a PCB substrate. After the preconcentration process, concentrated volume was recovered by a micro-syringe (10 μL) and injected into 100 μm width x 15 μm height straight channel for a measurement of intensity. The final concentration of sample A, B, and C was 5.91 nM (2.96 fold), 8.63 nM (4.32 fold), and 10.18 nM (5.09 fold), respectively. The calculated concentration ratio versus the concentration time for each sample is shown in solid line in Appendix Figure B. 2 (b). When compared with experimentally obtained values (dots marked with A, B, and C in the graph), it was confirmed that the recovery rate for the preconcentrated sample using this system was about 50 %. The detailed concentration time and experimental results are summarized in the Appendix Table B. 1.
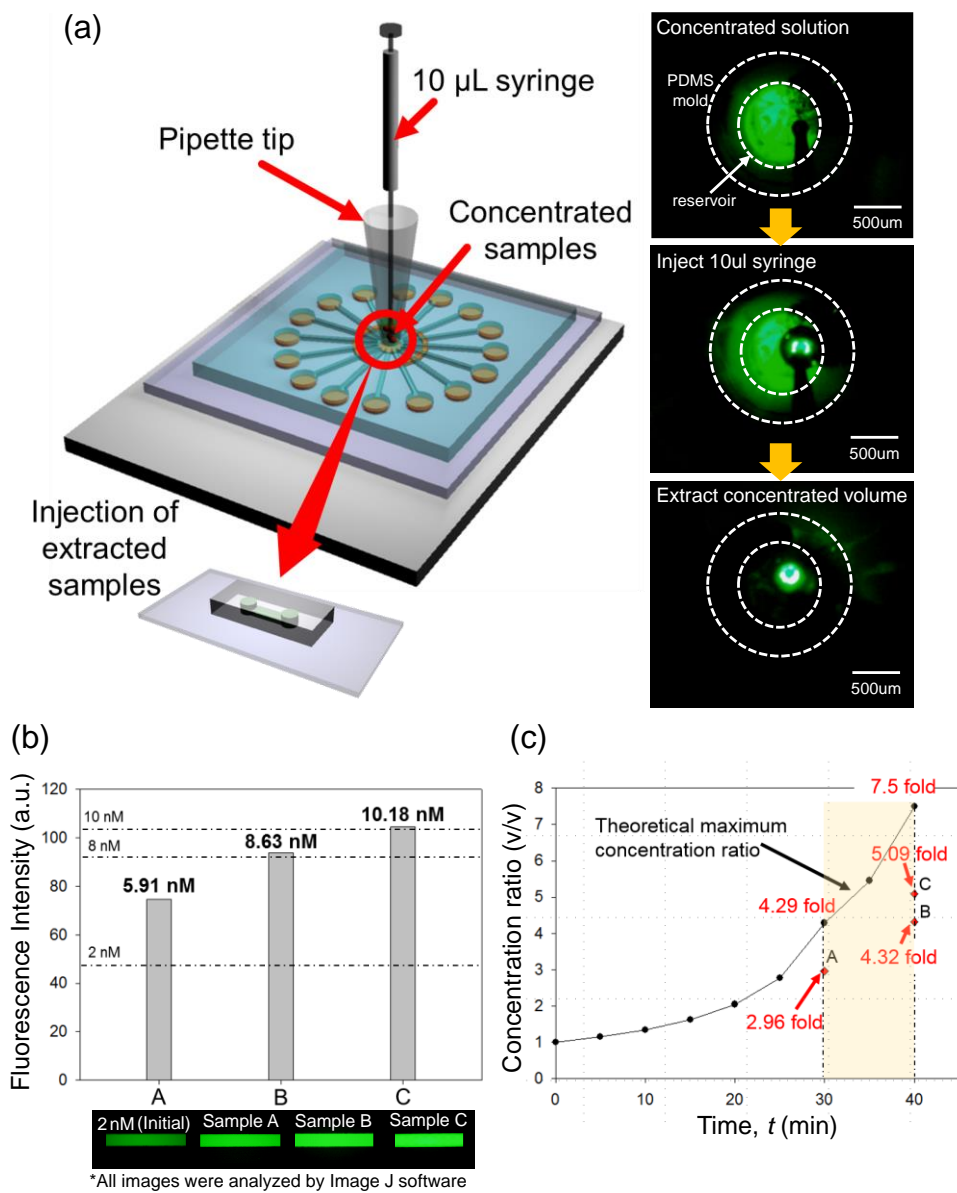
Appendix Figure B.2 (a) Preconcentration and extraction conceptual diagram of PCB substrate-based device (b) Results of preconcentrated and extracted fluorescence samples (c) Comparison between calculated values (solid line) and experimental values (dots).

83

	Operation time (min)	Recovered volume (µL)*	Final conc. (nM)**	Recovery ratio (%)
Sample A	30	7	5.91	69.1
Sample B	40	4	8.63	57.6
Sample C	40	2	10.18	49.1

*Initial volume: 30 µl, **Initial concentration: 2 nM

Appendix Table B.1 Operating time, extracted volume, and recovery ratio values for samples.

Bibliography

1.   Daw, R. and J. Finkelstein, *Insight: Lab on a chip.* Nature, 2006. **442**(7101): p. 367-418.

2.   van den Berg, A. and T.S. Lammerink, *Micro total analysis systems: microfluidic aspects, integration concept and applications.* Microsystem technology in chemistry and life science, 1998: p. 21-49.

3.   Reyes, D.R., et al., *Micro total analysis systems. 1. Introduction, theory, and technology.* Analytical chemistry, 2002. **74**(12): p. 2623-2636.

4.   Auroux, P.-A., et al., *Micro total analysis systems. 2. Analytical standard operations and applications.* Analytical chemistry, 2002. **74**(12): p. 2637-2652.

5.   Dittrich, P.S. and A. Manz, *Lab-on-a-chip: microfluidics in drug discovery.* Nature reviews Drug discovery, 2006. **5**(3): p. 210-218.

6.   Figeys, D. and D. Pinto, *Lab-on-a-chip: a revolution in biological and medical sciences.* 2000, ACS Publications.

7.   Di Carlo, D., *Inertial microfluidics.* Lab on a Chip, 2009. **9**(21): p. 3038-3046.

8.   Quake, S.R. and A. Scherer, *From micro-to nanofabrication with soft materials.* science, 2000. **290**(5496): p. 1536-1540.

9.   Sparreboom, W., A. van den Berg, and J.C. Eijkel, *Principles and applications of nanofluidic transport.* Nature nanotechnology, 2009. **4**(11): p. 713-720.

10.   Daiguji, H., P. Yang, and A. Majumdar, *Ion transport in nanofluidic channels.* Nano letters, 2004. **4**(1): p. 137-142.

11.   Morf, W.E., *The principles of ion-selective electrodes and of membrane transport.* 2012: Elsevier.

12.   Ko, S.H., et al., *Massively parallel concentration device for multiplexed immunoassays.* Lab on a Chip, 2011. **11**(7): p. 1351-1358.

13.   Choi, J., et al., *Selective preconcentration and online collection of charged molecules using ion concentration polarization.* RSC advances, 2015. **5**(81): p. 66178-66184.

14.   Baek, S., et al., *Dynamics of driftless preconcentration using ion concentration polarization leveraged by convection and diffusion.* Lab on a Chip, 2019. **19**(19): p. 3190-3199.

15.   Kim, S.J., et al., *Direct seawater desalination by ion concentration polarization.* Nature nanotechnology, 2010. **5**(4): p. 297-301.

16.   Kim, W., et al., *Experimental verification of simultaneous desalting and molecular preconcentration by ion concentration polarization.* Lab on a Chip, 2017. **17**(22): p. 3841-3850.

17.   Lee, H., et al., *Diffusiophoretic exclusion of colloidal particles for continuous water purification.* Lab on a Chip, 2018. **18**(12): p. 1713-1724.

18.   Nam, S., et al., *Experimental Verification of Overlimiting Current by Surface*

Conduction and Electro-Osmotic Flow in Microchannels. Physical Review Letters, 2015. **114**(11): p. 114501.

19. Kwon, S., H. Lee, and S.J. Kim, *Elimination of pseudo-negative conductance by coercive steady state in perm-selective ion transportation.* Biomicrofluidics, 2020. **14**(1): p. 014106.

20. Huh, K., et al., *Surface conduction and electroosmotic flow around charged dielectric pillar arrays in microchannels.* Lab on a Chip, 2020. **20**(3): p. 675-686.

21. Lee, S.-H., et al., *Sub-10 nm transparent all-around-gated ambipolar ionic field effect transistor.* Nanoscale, 2015. **7**(3): p. 936-946.

22. Lee, H., et al., *A concentration-independent micro/nanofluidic active diode using an asymmetric ion concentration polarization layer.* Nanoscale, 2017. **9**(33): p. 11871-11880.

23. Masliyah, J.H. and S. Bhattacharjee, *Electrokinetic and colloid transport phenomena*. 2006: John Wiley & Sons.

24. Behrens, S.H. and D.G. Grier, *The charge of glass and silica surfaces.* The Journal of Chemical Physics, 2001. **115**(14): p. 6716-6721.

25. Schoch, R.B., J. Han, and P. Renaud, *Transport phenomena in nanofluidics.* Reviews of modern physics, 2008. **80**(3): p. 839.

26. Kirby, B.J., *Micro-and nanoscale fluid mechanics: transport in microfluidic devices*. 2010: Cambridge university press.

27. Donnan, F.G., *Theory of membrane equilibria and membrane potentials in the presence of non-dialysing electrolytes. A contribution to physical-chemical physiology.* Journal of Membrane Science, 1995. **100**(1): p. 45-55.

28. Ostertag, L.M., et al., *Characterizing the hydrophobic-to-hydrophilic transition of electrolyte structuring in proton exchange membrane mimicking surfaces.* Physical Chemistry Chemical Physics, 2018. **20**(17): p. 11722-11729.

29. Consortium, I.H.G.S., *Finishing the euchromatic sequence of the human genome.* Nature, 2004. **431**(7011): p. 931.

30. Mitra, R.D. and G.M. Church, *In situ localized amplification and contact replication of many individual DNA molecules.* Nucleic Acids Research, 1999. **27**(24): p. e34-e39.

31. Metzker, M.L., *Sequencing technologies—the next generation.* Nature reviews genetics, 2010. **11**(1): p. 31-46.

32. Crowley, E., et al., *Liquid biopsy: monitoring cancer-genetics in the blood.* Nature reviews Clinical oncology, 2013. **10**(8): p. 472.

33. Bettegowda, C., et al., *Detection of circulating tumor DNA in early-and late-stage human malignancies.* Science translational medicine, 2014. **6**(224): p. 224ra24-224ra24.

34. Cohen, A., et al., *High-performance capillary electrophoretic separation of bases, nucleosides, and oligonucleotides: retention manipulation via micellar solutions and metal additives.* Analytical chemistry, 1987. **59**(7): p. 1021-1027.

35.   Grossman, P.D., *Factors affecting the performance of capillary electrophoresis separations: Joule heating, electroosmosis, and zone dispersion*. 1992: Academic Press, San Diego.

36.   Stellwagen, N.C., C. Gelfi, and P.G. Righetti, *The free solution mobility of DNA*. Biopolymers: Original Research on Biomolecules, 1997. **42**(6): p. 687-703.

37.   Viovy, J.-L., *Electrophoresis of DNA and other polyelectrolytes: Physical mechanisms*. Reviews of Modern Physics, 2000. **72**(3): p. 813.

38.   Meagher, R.J., et al., *End-labeled free-solution electrophoresis of DNA*. Electrophoresis, 2005. **26**(2): p. 331-350.

39.   Shagin, D.A., et al., *A high-throughput assay for quantitative measurement of PCR errors*. Scientific reports, 2017. **7**(1): p. 1-11.

40.   Clarke, L., et al., *PCR amplification introduces errors into mononucleotide and dinucleotide repeat sequences*. Molecular Pathology, 2001. **54**(5): p. 351.

41.   Kwak, R., S.J. Kim, and J. Han, *Continuous-flow biomolecule and cell concentrator by ion concentration polarization*. Analytical chemistry, 2011. **83**(19): p. 7348-7355.

42.   Lee, K., et al., *Enhancing the sensitivity of DNA detection by structurally modified solid-state nanopore*. Nanoscale, 2017. **9**(45): p. 18012-18021.

43.   Kwak, D.K., et al., *Probing the small-molecule inhibition of an anticancer therapeutic protein-protein interaction using a solid-state nanopore*. Angewandte Chemie International Edition, 2016. **55**(19): p. 5713-5717.

44.   Kim, D.-S., et al., *An FET-type charge sensor for highly sensitive detection of DNA sequence*. Biosensors and Bioelectronics, 2004. **20**(1): p. 69-74.

45.   Mani, A., T.A. Zangle, and J.G. Santiago, *On the propagation of concentration polarization from microchannel− nanochannel interfaces Part I: analytical model and characteristic analysis*. Langmuir, 2009. **25**(6): p. 3898-3908.

46.   Kim, S.J., L.D. Li, and J. Han, *Amplified electrokinetic response by concentration polarization near nanofluidic channel*. Langmuir, 2009. **25**(13): p. 7759-7765.

47.   Kim, S.J., et al., *Multi-vortical flow inducing electrokinetic instability in ion concentration polarization layer*. Nanoscale, 2012. **4**(23): p. 7406-7410.

48.   Rubinstein, I. and L. Shtilman, *Voltage against current curves of cation exchange membranes*. Journal of the Chemical Society, Faraday Transactions 2: Molecular and Chemical Physics, 1979. **75**: p. 231-246.

49.   Demekhin, E., N. Nikitin, and V. Shelistov, *Direct numerical simulation of electrokinetic instability and transition to chaotic motion*. Physics of Fluids, 2013. **25**(12): p. 122001.

50.   Zaltzman, B. and I. Rubinstein, *Electro-osmotic slip and electroconvective instability*. Journal of Fluid Mechanics, 2007. **579**: p. 173.

51.   Rubinstein, I. and B. Zaltzman, *Electro-osmotically induced convection at a permselective membrane*. Physical Review E, 2000. **62**(2): p. 2238.

52.   Rubinstein, S.M., et al., *Direct observation of a nonequilibrium electro-osmotic instability.* Physical review letters, 2008. **101**(23): p. 236101.

53.   Kim, S.J., et al., *Concentration polarization and nonlinear electrokinetic flow near a nanofluidic channel.* Physical review letters, 2007. **99**(4): p. 044501.

54.   Kim, S.J., Y.-A. Song, and J. Han, *Nanofluidic concentration devices for biomolecules utilizing ion concentration polarization: theory, fabrication, and applications.* Chemical Society Reviews, 2010. **39**(3): p. 912-922.

55.   Dydek, E.V., et al., *Overlimiting current in a microchannel.* Physical review letters, 2011. **107**(11): p. 118301.

56.   Plecis, A., et al., *Electropreconcentration with charge-selective nanochannels.* Analytical chemistry, 2008. **80**(24): p. 9542-9550.

57.   Cheow, L.F., et al., *Detecting kinase activities from single cell lysate using concentration-enhanced mobility shift assay.* Analytical chemistry, 2014. **86**(15): p. 7455-7462.

58.   Cheow, L.F. and J. Han, *Continuous signal enhancement for sensitive aptamer affinity probe electrophoresis assay using electrokinetic concentration.* Analytical chemistry, 2011. **83**(18): p. 7086-7093.

59.   Martins, D., et al., *Integration of multiplexed microfluidic electrokinetic concentrators with a morpholino microarray via reversible surface bonding for enhanced DNA hybridization.* Analytical chemistry, 2016. **88**(7): p. 3539-3547.

60.   Lee, J.H., et al., *Microfluidic concentration-enhanced cellular kinase activity assay.* Journal of the American Chemical Society, 2009. **131**(30): p. 10340-10341.

61.   Kim, J., et al., *Ion concentration polarization by bifurcated current path.* Scientific reports, 2017. **7**(1): p. 1-12.

62.   Lee, H., et al., *dCas9-mediated nanoelectrokinetic direct detection of target gene for liquid biopsy.* Nano letters, 2018. **18**(12): p. 7642-7650.

63.   Sternberg, S.H., et al., *DNA interrogation by the CRISPR RNA-guided endonuclease Cas9.* Nature, 2014. **507**(7490): p. 62-67.

64.   Abudayyeh, O.O., et al., *C2c2 is a single-component programmable RNA-guided RNA-targeting CRISPR effector.* Science, 2016. **353**(6299).

65.   Wu, X., et al., *Genome-wide binding of the CRISPR endonuclease Cas9 in mammalian cells.* Nature biotechnology, 2014. **32**(7): p. 670-676.

66.   Yakovlev, S., N.P. Balsara, and K.H. Downing, *Insights on the study of nafion nanoscale morphology by transmission electron microscopy.* Membranes, 2013. **3**(4): p. 424-439.

67.   Cho, I., et al., *Non-negligible diffusio-osmosis inside an ion concentration polarization layer.* Physical review letters, 2016. **116**(25): p. 254501.

68.   Lee, J.H., Y.-A. Song, and J. Han, *Multiplexed proteomic sample preconcentration device using surface-patterned ion-selective membrane.* Lab on a Chip, 2008. **8**(4): p. 596-601.

69.   Cheow, L.F., et al., *Increasing the sensitivity of enzyme-linked*

immunosorbent assay using multiplexed electrokinetic concentrator. Analytical chemistry, 2010. **82**(8): p. 3383-3388.

70. Yossifon, G., et al., *Nonlinear current-voltage characteristics of nanochannels.* Physical Review E, 2009. **79**(4): p. 046305.

71. Stein, D., M. Kruithof, and C. Dekker, *Surface-charge-governed ion transport in nanofluidic channels.* Physical Review Letters, 2004. **93**(3): p. 035901.

72. Milanova, D., et al., *Electrophoretic mobility measurements of fluorescent dyes using on-chip capillary electrophoresis.* Electrophoresis, 2011. **32**(22): p. 3286-3294.

73. Chun, H., *Electropreconcentration, gate injection, and capillary electrophoresis separation on a microchip.* Journal of Chromatography A, 2018. **1572**: p. 179-186.

74. Merhari, L., *Hybrid nanocomposites for nanotechnology.* 2009: Springer.

75. Jinek, M., et al., *Structures of Cas9 endonucleases reveal RNA-mediated conformational activation.* Science, 2014. **343**(6176).

76. Shibata, M., et al., *Real-space and real-time dynamics of CRISPR-Cas9 visualized by high-speed atomic force microscopy.* Nature communications, 2017. **8**(1): p. 1-9.

77. Sun, W., et al., *Self-assembled DNA nanoclews for the efficient delivery of CRISPR–Cas9 for genome editing.* Angewandte Chemie, 2015. **127**(41): p. 12197-12201.

78. Keyser, U.F., et al., *Direct force measurements on DNA in a solid-state nanopore.* Nature Physics, 2006. **2**(7): p. 473-477.

79. Teraoka, I., *Polymer solutions in confining geometries.* Progress in polymer science, 1996. **21**(1): p. 89-149.

80. Kobayashi, S., et al., *EGFR mutation and resistance of non–small-cell lung cancer to gefitinib.* New England Journal of Medicine, 2005. **352**(8): p. 786-792.

81. Toyooka, S., K. Kiura, and T. Mitsudomi, *EGFR mutation and response of lung cancer to gefitinib.* N Engl J Med, 2005. **352**(20): p. 2136.

82. Arora, A., et al., *Latest developments in micro total analysis systems.* Analytical chemistry, 2010. **82**(12): p. 4830-4847.

83. Khandurina, J., et al., *Microfabricated porous membrane structure for sample concentration and electrophoretic analysis.* Analytical Chemistry, 1999. **71**(9): p. 1815-1819.

84. Song, S., A.K. Singh, and B.J. Kirby, *Electrophoretic concentration of proteins at laser-patterned nanoporous membranes in microchips.* Analytical Chemistry, 2004. **76**(15): p. 4589-4592.

85. Zularisam, A., A. Ismail, and R. Salim, *Behaviours of natural organic matter in membrane filtration for surface water treatment—a review.* Desalination, 2006. **194**(1-3): p. 211-231.

86. Di Carlo, D., et al., *Continuous inertial focusing, ordering, and separation of particles in microchannels.* Proceedings of the National Academy of

Sciences, 2007. **104**(48): p. 18892-18897.

87. Connacher, W., et al., *Micro/nano acoustofluidics: materials, phenomena, design, devices, and applications.* Lab on a Chip, 2018.

88. Vigolo, D., et al., *Thermophoresis: microfluidics characterization and separation.* Soft Matter, 2010. **6**(15): p. 3489-3493.

89. Yang, M. and M. Ripoll, *Thermoosmotic microfluidics.* Soft matter, 2016. **12**(41): p. 8564-8573.

90. Jung, B., R. Bharadwaj, and J.G. Santiago, *On-chip millionfold sample stacking using transient isotachophoresis.* Analytical chemistry, 2006. **78**(7): p. 2319-2327.

91. Bottenus, D., et al., *10000-fold concentration increase of the biomarker cardiac troponin I in a reducing union microfluidic chip using cationic isotachophoresis.* Lab on a Chip, 2011. **11**(5): p. 890-898.

92. Lichtenberg, J., E. Verpoorte, and N.F. de Rooij, *Sample preconcentration by field amplification stacking for microchip-based capillary electrophoresis.* Electrophoresis, 2001. **22**(2): p. 258-271.

93. Wei, W., G. Xue, and E.S. Yeung, *One-step concentration of analytes based on dynamic change in pH in capillary zone electrophoresis.* Analytical chemistry, 2002. **74**(5): p. 934-940.

94. Arnett, S.D. and C.E. Lunte, *Investigation of the mechanism of pH-mediated stacking of anions for the analysis of physiological samples by capillary electrophoresis.* Electrophoresis, 2003. **24**(11): p. 1745-1752.

95. Beard, N.P., C.X. Zhang, and A.J. demello, *In-column field-amplified sample stacking of biogenic amines on microfabricated electrophoresis devices.* Electrophoresis, 2003. **24**(4): p. 732-739.

96. Jung, B., R. Bharadwaj, and J.G. Santiago, *Thousandfold signal increase using field-amplified sample stacking for on-chip electrophoresis.* Electrophoresis, 2003. **24**(19-20): p. 3476-3483.

97. Son, S.Y., et al., *Engineered nanofluidic preconcentration devices by ion concentration polarization.* BioChip Journal, 2016. **10**(4): p. 251-261.

98. Wang, Y.-C., A.L. Stevens, and J. Han, *Million-fold Preconcentration of Proteins and Peptides by Nanofluidic Filter.* Analytical Chemistry, 2005. **77**(14): p. 4293-4299.

99. Fu, L.M., et al., *Sample preconcentration from dilute solutions on micro/nanofluidic platforms: A review.* Electrophoresis, 2018. **39**(2): p. 289-310.

100. Chen, Y.-Y., et al., *Preconcentration of diluted mixed-species samples following separation and collection in a micro–nanofluidic device.* Biomicrofluidics, 2016. **10**(1): p. 014119.

101. Park, S., et al., *High-throughput on-chip leukemia diagnosis.* International journal of laboratory hematology, 2013. **35**(5): p. 480-490.

102. Han, S.I., et al., *High-ionic-strength pre-concentration via ion concentration polarization for blood-based biofluids.* Sensors and Actuators B: Chemical, 2018. **268**: p. 485-493.

103. Ouyang, W., et al., *Deciphering ion concentration polarization-based electrokinetic molecular concentration at the micro-nanofluidic interface: theoretical limits and scaling laws.* Nanoscale, 2018.

104. Hong, S.A., et al., *Electrochemical detection of methylated DNA on a microfluidic chip with nanoelectrokinetic pre-concentration.* Biosensors and Bioelectronics, 2018. **107**: p. 103-110.

105. Lee, D., et al., *spontaneous selective preconcentration Leveraged by Ion exchange and Imbibition through Nanoporous Medium.* Scientific reports, 2019. **9**(1): p. 2336.

106. Pu, Q., et al., *Ion-Enrichment and Ion-Depletion Effect of Nanochannel Structures.* Nano Letters, 2004. **4**: p. 1099-1103.

107. Kim, S.J., et al., *Concentration Polarization and Nonlinear Electrokinetic Flow near Nanofluidic Channel.* Physical Review Letters, 2007. **99**: p. 044501.

108. Sohn, S., et al., *Surface Conduction in a Microchannel.* Langmuir, 2018. **34**(26): p. 7916-7921.

109. Chang, H.-C. and G. Yossifon, *Understanding electrokinetics at the nanoscale: A perspective.* Biomicrofluidics, 2009. **3**: p. 012001.

110. Yossifon, G. and H.-C. Chang, *Selection of nonequilibrium overlimiting currents: Universal depletion layer formation dynamics and vortex instability.* Physical Review Letters, 2008. **101**: p. 254501.

111. Park, S., et al., *Capillarity ion concentration polarization as spontaneous desalting mechanism.* Nat Commun, 2016. **7**: p. 11223.

112. Druzgalski, C.L., M.B. Andersen, and A. Mani, *Direct numerical simulation of electroconvective instability and hydrodynamic chaos near an ion-selective surface.* Physics of Fluids, 2013. **25**(11): p. 110804.

113. Andersen, M.B., et al., *Current-Induced Membrane Discharge.* Physical Review Letters, 2012. **109**(10).

114. Rubinstein, I. and B. Zaltzman, *Extended space charge in concentration polarization.* Advances in Colloid and Interface Science, 2010. **159**(2): p. 117-129.

115. Yossifon, G., et al., *Nonlinear current-voltage characteristics of nanochannels.* Physical Review E, 2009. **79**(4).

116. Choi, J., et al., *Selective preconcentration and online collection of charged molecules using ion concentration polarization.* RSC Advances, 2015. **5**(81): p. 66178-66184.

117. Chen, C.-H., et al., *Enhancing protease activity assay in droplet-based microfluidics using a biomolecule concentrator.* Journal of the American Chemical Society, 2011. **133**(27): p. 10368-10371.

118. Wang, Y.-C. and J. Han, *Pre-binding dynamic range and sensitivity enhancement for immuno-sensors using nanofluidic preconcentrator.* Lab on a Chip, 2008. **8**(3): p. 392-394.

119. Ko, S.H., et al., *Nanofluidic preconcentration device in a straight microchannel using ion concentration polarization.* Lab on a Chip, 2012.

12(21): p. 4472-4482.

120. Huang, K.D. and R.J. Yang, *A nanochannel-based concentrator utilizing the concentration polarization effect.* Electrophoresis, 2008. **29**(24): p. 4862-4870.

121. Jia, M. and T. Kim, *Multiphysics Simulation of Ion Concentration Polarization Induced by a Surface-Patterned Nanoporous Membrane in Single Channel Devices.* Analytical Chemistry, 2014. **86**(20): p. 10365-10372.

122. Kim, M., M. Jia, and T. Kim, *Ion concentration polarization in a single and open microchannel induced by a surface-patterned perm-selective film.* Analyst, 2013. **138**(5): p. 1370-1378.

123. Sung Hee Ko, S.J.K., Jongyoon Han, *Method for Building Massively-Parallel Preconcentration Device for Multiplexed, High-Throughput Applications* M.I.o. Technology, Editor. 2010: United State of America.

124. Andersen, M.B., et al., *Confinement effects on electroconvective instability.* Electrophoresis, 2017. **38**(5): p. 702-711.

125. Alizadeh, S. and A. Mani, *Multiscale Model for Electrokinetic Transport in Networks of Pores, Part I: Model Derivation.* Langmuir, 2017. **33**(25): p. 6205-6219.

126. Davidson, S.M., M.B. Andersen, and A. Mani, *Chaotic Induced-Charge Electro-Osmosis.* Physical Review Letters, 2014. **112**: p. 128302.

127. Rubinstein, S.M., et al., *Direct Observation of a Nonequilibrium Electro-Osmotic Instability* Physical Review Letters, 2008. **101**: p. 236101.

128. Pundik, T., I. Rubinstein, and B. Zaltzman, *Bulk electroconvection in electrolyte.* Physical Review E, 2005. **72**(061502): p. 061502.

129. Yossifon, G., P. Mushenheim, and H.C. Chang, *Controlling nanoslot overlimiting current with the depth of a connecting microchamber.* Europhysics Letters, 2010. **90**(6).

130. Yossifon, G., et al., *Eliminating the limiting-current phenomenon by geometric field focusing into nanopores and nanoslots.* Physical Review E, 2010. **81**(4).

131. Dydek, E.V., et al., *Overlimiting Current in a Microchannel.* Physical Review Letters, 2011. **107**: p. 118301.

132. Kim, J., et al., *Ion Concentration Polarization by Bifurcated Current Path.* Scientific Reports, 2017. **7**(1): p. 5091.

133. Kim, K., et al., *Stabilization of ion concentration polarization layer using micro fin structure for high-throughput applications.* Nanoscale, 2017. **9**(10): p. 3466-3475.

134. Kim, P., et al., *Stabilization of ion concentration polarization using a heterogeneous nanoporous junction.* Nano Letters, 2010. **10**: p. 16-23.

135. Scarff, B., C. Escobedo, and D. Sinton, *Radial sample preconcentration.* Lab on a Chip, 2011. **11**(6): p. 1102-1109.

136. Lee, J.H., Y.-A. Song, and J. Han, *Multiplexed Proteomic Sample Preconcentration Device Using Surface-Patterned Ion-Selective Membrane*

Lab on a Chip, 2008. **8**: p. 596 - 601.

137.   Fosdick, S.E., et al., *Bipolar Electrochemistry.* Angewandte chemie International Edition, 2013. **52**(40): p. 10438-10456.

138.   Knust, K.N., et al., *Electrochemically Mediated Seawater Desalination.* Angewandte chemie International Edition, 2013. **52**(31): p. 8107-8110.

139.   Sze, A., et al., *Zeta-potential measurement using the Smoluchowski equation and the slope of the current–time relationship in electroosmotic flow.* Journal of colloid and interface science, 2003. **261**(2): p. 402-410.

140.   Bruus, H., *Theoretical microfluidics*. Vol. 18. 2008: Oxford university press Oxford.

141.   Schellman, J.A. and D. Stigter, *Electrical double layer, zeta potential, and electrophoretic charge of double-stranded DNA.* Biopolymers: Original Research on Biomolecules, 1977. **16**(7): p. 1415-1434.

142.   Zangle, T.A., A. Mani, and J.G. Santiago, *Theory and experiments of concentration polarization and ion focusing at microchannel and nanochannel interfaces.* Chemical Society Reviews, 2010. **39**: p. 1014-1035.

143.   Kwak, R. and J. Han, *Half-Cell Ion Concentration Polarization on Nafion-Coated Electrode.* The journal of physical chemistry letters, 2018. **9**(11): p. 2991-2999.

144.   Kaye, G.W.C. and T.H. Laby, *Tables of physical and chemical constants.* Harlow: Longman's, London, 1995.

145.   Haff, L.A. and I.P. Smirnov, *Single-nucleotide polymorphism identification assays using a thermostable DNA polymerase and delayed extraction MALDI-TOF mass spectrometry.* Genome research, 1997. **7**(4): p. 378-388.

146.   Ross, P., et al., *High level multiplex genotyping by MALDI-TOF mass spectrometry.* Nature biotechnology, 1998. **16**(13): p. 1347.

147.   Singh, M., et al., *Inkjet printing—process and its applications.* Advanced materials, 2010. **22**(6): p. 673-685.

148.   Calvert, P., *Inkjet printing for materials and devices.* Chemistry of materials, 2001. **13**(10): p. 3299-3305.

Abstract in Korean

소형화에서 오는 높은 시료 분석 효율과 시스템 제어의 용이함 등의 장점으로 인해 마이크로 유체역학은 1990년대 이후로 각광받고 있었다. 한편 나노공정기술의 발전으로 마이크로/나노유체역학 시스템에 대한 연구가 가속화되었다. 마이크로미터 아래 영역에서는 다른 영역에서 관찰되지 않았던 새로운 물리 화학적 현상들이 발견되었는데, 이 중 EDL overlap에 의한 선택적 투과성이 가장 중요한 특징으로 손꼽히고 있다. 이 선택적 투과성을 이용한 마이크로/나노유체역학 시스템을 통해 분석장치, 질병 진단, 담수화, 에너지 하베스팅 등 다양한 응용 분야에 대한 연구가 진행되고 있다. 본 학위논문에서는 혈액암의 종류인 EGFR L858R 돌연변이에 대한 검출을 시도하였으며, 다운스트림 분석을 위한 효율적인 형태의 장치를 제안하였다.

먼저, 이온 농도 분극 현상과 특정 염기서열에 결합하는 dCas9 단백질을 이용하여 타겟 혈액암 진단 연구를 수행하였다. 암 진단은 조기 진단이 중요하기 때문에 최근 현장 의료 진단 방식에 대한 연구가 활발히 진행되고 있다. 다양한 진단 기술들 중 연쇄중합반응 방식이 가장 흔히 쓰이는데 비용과 시간이 많이 드는 등의 단점이 있다. 따라서 대안으로써 이온 농도 분극 현상과 특정 DNA와 결합하는 dCas9을 이용한 타겟 DNA 검출 연구가 발표된바 있다. 이에 대한 후속 연구로써 본 연구에서는 혈액암 중 폐암의 원인이 되는 마커 (EGFR L858R)을 전체 시료 함유량 1 %까지 낮춰가며 검출에 성공하였고 이 때, dCas9 단백질의 타겟 결합율은 함유량에 큰 상관관계 없이 약 25 %를 유지하였다. 또한, 하나의 염기서열만 다른 경우에도 본 연구의 방법으로 성공적으로 검출할 수 있음을 보였다. 이 플랫폼을 통해 향후

on/off 방식의 혈액암 조기진단 칩으로 활용될 수 있을 것이라 기대된다.

  다음으로, 효율적인 구조로 디자인된 마이크로/나노유체역학 방식의 농축 및 추출 장치를 고안했다. 나노유체역학 플랫폼에서의 다양한 농축기술 중 이온 농도 분극 현상을 이용한 농축 방식은 높은 농축율과 복잡한 버퍼 교환 과정이 필요없는 등의 장점으로 많이 연구되고 있다. 하지만 기존의 이온 농도 분극 현상 농축방식으로는 농축된 샘플을 추출하는 것이 어려웠다. 이를 해결하기 위해 본 연구에서는 간단하게 원형으로 배치된 채널 구조를 통해 농축된 샘플을 추출할 수 있었다. 원형으로 배치된 각각의 채널에서 농축이 진행되면서 용매는 밖으로 빠져나가고, 농축된 샘플을 가운데에 꼽힌 파이펫 팁을 회수해줌으로써 얻어낼 수 있었다. 간단하면서 저가형의 공정을 위해 사무용 프린터기를 개조하여 나노막을 패터닝하는데 성공하였다. 폴리스티렌 파이클, 형광입자, DNA 를 이용해 농축 및 추출 실험을 하였으며 각각 85.5 %, 79.0 %, 51.3 %의 회수율을 얻었다. 또한, 슈퍼 잉크젯 프린터를 이용해 전극을 패터닝하여 나노막 대신 이온 선택성을 구현하였다. Faradaic 반응을 이용한 전극 프린팅 디바이스를 통해 양전하 입자, 음전하 입자 모두 성공적으로 농축하는데 성공하였다. 본 연구에서 고안한 방사형 농축–추출 장치를 통해 실제 임상 환경 등에 적용할 수 있을 것이라 기대된다.

Acknowledgements